High fat diet ameliorates the mitochondrial cardiomyopathy of CHCHD10 mutant mice

Nneka Southwell[1,2], Dazhi Zhao[1], Nicole M. Sayles[1,2], Jalia Dash[1], Keigo Fujita[3], Marilena D'Aurelio[1], Giovanni Manfredi[1], Hibiki Kawamata[1*]

[1]Feil Family Brain and Mind Research Institute, Weill Cornell Medicine, 407 East 61st Street, New York, NY 10065. [2]Neuroscience Graduate Program, Weill Cornell Graduate School of Medical Sciences, 1300 York Ave, New York, NY 10065. [3]Millburn High School, 462 Millburn Ave, Millburn NJ 07041.

*Correspondence to Hibiki Kawamata: hik2004@med.cornell.edu

Abstract

Mutations in CHCHD10, a mitochondrial protein with still undefined function, are associated with dominant multi-system mitochondrial diseases. CHCHD10 knock-in mice harboring a heterozygous S55L mutation (equivalent to the human pathogenic S59L mutation) develop a fatal mitochondrial cardiomyopathy. The heart of S55L knock-in mice shows extensive metabolic rewiring triggered by proteotoxic mitochondrial integrated stress response (mtISR). In the mutant heart, mtISR initiates well before the onset of mild bioenergetic impairments and is associated with a shift from fatty acid oxidation to glycolytic metabolism and widespread metabolic imbalance. We tested therapeutic interventions to counteract the metabolic rewiring and ameliorate the metabolic imbalance. Heterozygous S55L mice were subjected to chronic high fat diet (HFD) to decrease insulin sensitivity and glucose uptake and enhance fatty acid utilization in the heart. Metabolomics and gene expression profiles demonstrated that HFD achieved an increase of fatty acid utilization in the heart accompanied by a decrease in cardiomyopathy markers. Surprisingly, HFD also decreased the accumulation of aggregated CHCHD10 in the S55L heart. Importantly, HFD increased the survival of mutant female mice exposed to acceleration of the mitochondrial cardiomyopathy associated with pregnancy. Our findings indicate that metabolic alterations can be effectively targeted for therapeutic intervention in mitochondrial cardiomyopathies associated with proteotoxic stress.

Abbreviations: high fat diet (HFD), control diet (CD), wildtype (WT), coiled-helix-coiled-helix-domain containing 10 (CHCHD10), mutant S59L CHCHD10 (Het), fatty acid (FA), fatty acid oxidation (FAO), mitochondrial integrated stress response (mtISR), amyotrophic lateral sclerosis (ALS), frontotemporal dementia (FTD), frataxin (FXN), central nervous system (CNS)

Key words: high fat diet, mitochondrial myopathies, cardiac hypertrophy, CHCHD10, frataxin

Introduction

Mitochondria are crucial to life and their impairment contributes to the pathogenesis of many genetic diseases associated with mutations in nuclear or mitochondrial DNA encoded genes. The discovery of mutations in CHCHD10 in autosomal dominant familial amyotrophic lateral sclerosis and frontotemporal dementia (ALS-FTD) (Bannwarth *et al*, 2014; Johnson *et al*, 2014; Muller *et al*, 2014) supports the role of mitochondrial dysfunction in the pathogenesis of hereditary neurodegenerative diseases. Although considered rare overall (Chia *et al*, 2018), mutations in CHCHD10 are increasingly being identified in families affected by ALS and other neurodegenerative conditions, such as FTD and Charcot Marie Tooth disease, as well as

myopathy and cardiomyopathy (Zhou *et al*, 2017). The normal function of CHCHD10 is still under investigation, but studies have shown that it associates with its paralog protein CHCHD2 and several other mitochondrial proteins, such as P32 (Burstein *et al*, 2018), mitofilin (Genin *et al*, 2018), and prohibitin (Genin *et al*, 2022). Individual ablation of CHCHD10 (Anderson *et al*, 2019; Liu *et al*, 2020) or CHCHD2 (Nguyen *et al*, 2021) in mice modestly impairs mitochondrial function, while knock out of both proteins causes mitochondrial alterations (Liu *et al.*, 2020), indicating that the two paralog proteins can complement each other functionally. Together with the autosomal dominant nature of CHCHD10 mutations, these data suggest that CHCHD10-related diseases are caused by a pathogenic gain of toxic function, rather than a loss of function.

S55L (S59L in human) knock-in mice genetically recapitulate the first described pathogenic human mutation in CHCHD10 (Bannwarth *et al.*, 2014). These mice develop myopathy, neuromuscular junction denervation, mitochondrial abnormalities in neurons, and premature death due to cardiomyopathy (Anderson *et al.*, 2019; Genin *et al*, 2019; Liu *et al.*, 2020). More recently, a knock-in mouse harboring a G58R was also shown to develop a fatal myopathy and cardiomyopathy phenotype (Shammas *et al*, 2022). CHCHD10 protein aggregates have been described in all of these animal models of pathogenic human CHCHD10 mutations. Aggregation of mutant CHCHD10 results in the activation of a mitochondrial integrated stress response (mtISR) and an extensive metabolic rewiring (Anderson *et al.*, 2019; Shammas *et al.*, 2022). Specifically, we showed that the heart of the S55L mice becomes highly dependent on glucose metabolism, at the expense of fatty acid oxidation (FAO) (Sayles *et al*, 2022). During early postnatal heart development, cardiomyocyte energy metabolism shifts from glucose utilization to FAO. However, in pathologic conditions, such as pressure overload, the diseased heart relies heavily on glucose uptake and glycolysis for energy production (Ritterhoff & Tian, 2017). Glucose dependance was also demonstrated in a mouse model of cardiomyopathy caused by conditional ablation of the mitochondrial protease Yme1L selectively in the heart, but a high fat diet (HFD), which decreases insulin sensitivity and forces the utilization of fatty acids, attenuated cardiac dysfunction (Wai *et al*, 2015).

Based on our current understanding of the effects of CHCHD10 mutations on metabolism, we propose that rewiring towards glycolysis has detrimental effects associated with metabolite imbalance, including nucleotides and glutathione (Sayles *et al.*, 2022). Hence, we hypothesized that modulation of metabolic substrate preference could be beneficial for CHCHD10-related disease. To test this hypothesis, we subjected heterozygote S55L mice (Het) to long-term HFD and analyzed transcriptomic, metabolomic, and lipidomic profiles in the heart and the central nervous system (CNS). We found that HFD dramatically modifies the metabolism of heart and

improves cardiac stress in mutant mice. Furthermore, HFD significantly prolongs the lifespan of female Het mice under conditions of hemodynamic stress induced by pregnancy. Unexpectedly, HFD also decreased the accumulation of CHCHD10 aggregates in mitochondria. These findings support the use of metabolic therapies for mitochondrial disorders associated with proteotoxicity and mtISR.

Results

HFD started *in utero* has different transcriptional and metabolic effects in adult wild type (WT) and heterozygous CHCHD10^{S55L} (Het) hearts

Since the S55L (in human S59L) CHCHD10 mutation leads to hypertrophic mitochondrial cardiomyopathy with altered energy metabolism (Anderson *et al.*, 2019; Sayles *et al.*, 2022), we reasoned that HFD could be effective in relieving the cardiomyopathic phenotype in Het mice. To maximize the effect of the HFD treatment, forcing fatty acid (FA) utilization in the heart, we tested a paradigm of long-term treatment, whereby mice are exposed to HFD from *in utero* to adulthood, by feeding pregnant dams with HFD and continuing the diet after weaning. Since Het mice manifest cardiomyopathy and stress markers by 75 days of age (Sayles *et al.*, 2022), we harvested tissues from Het and wild-type (WT) mice on control diet (CD) or HFD at P75 and performed unbiased metabolomics and transcriptomic analyses.

As we previously observed, many genes were significantly different between Het and WT hearts on CD (4,621 DEGs with padj. <0.05, Fig. 1A). Remarkably, HFD had much larger transcriptional effects in Het hearts (4,838 DEGs, Fig. 1B) than in WT hearts (33 DEGs, Fig. 1C), suggesting that mutant hearts respond to HFD differently than WT hearts. Next, we analyzed transcriptional differences between HFD Het and CD WT hearts to identify changes that rendered mutants more similar to normal hearts, and therefore with putative beneficial effects. Compared to CD Het vs. CD WT (Fig. 1A), there were less DEGs when Het mice were in HFD (1,082 DEGs, Fig. 1D), suggesting that HFD normalizes many genes altered by the mutation. As expected, among the upregulated pathways enriched in Het vs. WT hearts in CD, we found cardiac and muscle hypertrophy in response to stress (Fig. 1E). However, in HFD Het mice, these pathways were downregulated compared to Het mice in CD (Fig. 1F), suggesting that in Het mice HFD decreases cardiac stress. Individual genes comprising this pathway, including *Myh6*, *Nppb*, and *Atp2b4*, were decreased by HFD in Het hearts (Fig. 1G).

There were significant differences in metabolite abundance between Het and WT hearts on CD (64 metabolites with Log2 fold change >1; p<0.05, Fig. 2A). While HFD induced metabolic changes in both Het (142 metabolites with p<0.05, Fig. 2B) and WT hearts (147 metabolites with

$p<0.05$, Fig. 2C), most of these metabolites did not overlap (Fig. 2D). Enrichment analysis of all significant ($p<0.05$), non-overlapping metabolites in HFD showed several differences between WT and Het hearts. Notable pathways enriched only in WT hearts were glycolysis, citric acid cycle, and carnitine biosynthesis (Fig. 2E, F). Pathways enriched only in Het HFD, included upregulation of phosphatidylcholine and phosphatidylethanolamine biosynthesis and downregulation of cardiolipin biosynthesis (Fig. 2G, H). A heatmap of the 50 most differentially represented metabolites highlighted groups of molecules which were different based on genotype and others that differed based on diet, and a group that depended on both genotype and diet (Fig. 2I). Interestingly, most of these metabolites responded differently to HFD in WT and Het hearts. Among these, a subset was changed by HFD only in Het hearts and acquired a profile more alike WT in CD. Taken together, metabolomics and transcriptomics data indicate that HFD had significant and distinct effects in Het and WT hearts and that metabolic changes induced by HFD in Het were associated with decreased cardiac stress markers.

To further understand the changes that drive the metabolic effects of HFD in Het and WT hearts, we examined the expression of specific genes encoding for enzymes and transporters, as well as their substrates and products identified by metabolomics. The expression of key regulatory proteins in FAO, such as the plasma membrane FA transporter *Fatp1* (Fig. 3A) was decreased in Het in CD relative to WT hearts (Fig. 3B), but was increased by HFD to levels comparable to WT. Moreover, expression of *Cpt1* and *Cpt2*, which transport FA into mitochondria for oxidation (Fig. 3A), were also decreased in Het hearts and overall increased by HFD (Fig. 3B). The expression of *Hadha* subunit of the trifunctional protein, a crucial step of long chain FAO (Fig. 3A) and cardiolipin remodeling in the heart, was severely decreased in Het hearts and restored by HFD (Fig. 3B). Interestingly, HADHA deficiency has been associated with neonatal syndromes characterized by hypoglycemia, myopathy, and cardiomyopathy (Prasun *et al*, 1993). The levels of the insulin-sensitive glucose transporter *Glut4* were increased in Het hearts and significantly decreased by HFD (Fig. 3C). Hexokinase isoform 1 (*Hk1*) was decreased in Het hearts and increased by HFD (Fig. 3C). Glucose levels were reduced in Het hearts and restored by HFD (Fig. 3D). The levels of phosphoenolpyruvate were increased by HFD in Het hearts, whereas pyruvate was decreased (Fig. 3D). Taken together, these findings suggest that HFD favors FA utilization in Het hearts.

We previously demonstrated that cardiomyopathy in Het mice is associated with mtISR, leading to upregulation of the serine one-carbon metabolism (Anderson *et al.*, 2019; Sayles *et al.*, 2022). We confirmed these findings in Het hearts on CD, showing elevation of the expression of several enzymes of this pathway, including *Psat1*, *Mthfd1l*, *Mthfd2*, *Mthfr*, and showed that HFD

decreases their levels (Fig. 3E,F). Analyses of metabolites also confirmed rewiring of the serine one-carbon metabolism in Het hearts on CD compared to WT with elevation of serine, glycine, methionine, cystathionine, GSSG, and GSH and decrease of S-Adenosyl-L-homocysteine (SAH) (Fig. 3E,G). Several of these metabolites were differentially affected by HFD in Het and WT hearts. For example, SAH was decreased in WT but not in Het, resulting in similar levels in the two genotypes. Conversely, phosphoserine was only elevated by HFD in WT and not in Het hearts. These results suggest that HFD can modulate the metabolic rewiring induced by mtISR. We also found that Het had decreased levels of adenosine, which were restored by HFD (Fig. 3H). This is potentially significant for the therapeutic role of HFD, since adenosine plays important roles not only energy metabolism, but also in cardioprotection (Kitakaze & Hori, 2000).

Next, we investigated heart lipidomic profiles. The class of lipids was most changed in Het hearts relative to WT under CD and in response to HFD were phospholipids, whereas no differences in triglycerides and cholesterol esters were associated with genotype or diet (Supplementary Fig. 1). Overall, there were many phospholipids that were affected by genotype but not by diet, while others were only affected by HFD in Het but not in WT hearts (Fig. 4A, B). Moreover, among the different phospholipids, cardiolipin (CL), one of the most abundant mitochondrial inner membrane lipids, was of particular interest due to its role in the maintenance of mitochondria structure and function. Several CLs were differentially represented between WT and Het hearts and responded to HFD in one genotype but not the other (Fig. 4C). Transcriptomic analysis of genes involved in lipolysis and phospholipid biosynthesis (Fig. 4D) showed differences, mostly downregulation, in the expression of several enzymes in Het compared to WT in CD, which were restored by HFD (Fig. 4E). These results show that Het hearts have altered phospholipid levels, which can contribute to mitochondrial dysfunction and cardiomyopathy and that HFD modulates phospholipid metabolism in the heart.

HFD started *in utero* has different metabolic effects in adult WT and Het spinal cords

Since the S59L CHCHD10 mutation is associated with familial ALS (Bannwarth *et al.*, 2014) and the mouse model of the disease presents spinal motor neuron alterations and muscle denervation (Anderson *et al.*, 2019), we investigated the transcriptional and metabolic effects of HFD in the spinal cord of mice treated with HFD at P75. At this age, there were no significant transcriptional changes between Het and WT spinal cord (Supplementary Fig. 2A), and only a handful of genes reached statistical significance comparing Het spinal cord in HFD and CD (Supplementary Fig. 2B). Also, no changes were found in HFD WT vs. CD WT spinal cord (Supplementary Fig. 2C). On the other hand, we detected differences in the metabolite profiles of

Het and WT spinal cords (Fig. 5A). HFD had different effects on the metabolomics of the spinal cord in Het and WT animals (Fig. 5B-D) with a higher number of metabolites altered in WT spinal cord.

The upregulated metabolites were mostly different in Het and WT, whereas the downregulated largely overlapped (Fig. 5E). The metabolites upregulated only in Het spinal cord were enriched in several pathways including amino acids, nucleotide, and phospholipids (Fig. 5F). Pathways enriched in WT only included citric acid cycle, riboflavin, and glucose metabolism, among others (Fig. 5G). Very few metabolites were downregulated uniquely in one group, while the common downregulated pathways in Het and WT comprised carnitine synthesis, β-oxidation, and electron transfer chain (Fig. 5H). Together these results indicate that HFD has virtually no global transcriptional effects in the spinal cord, at least at the age investigated (P75). The presence of metabolic changes in the absence of transcriptional differences, suggest that differentially represented metabolites may reach the CNS from the periphery through the circulation.

Metabolic phenotyping studies underscore different responses to HFD in Het and WT mice

To assess the phenotypic outcomes of HFD, we performed a longitudinal study in Het and WT mice on HFD or CD started *in utero* and continued until mice reached 1 year of age. As previously reported (Anderson *et al.*, 2019) the body weight of both female and male Het on CD mice ceased to increase beyond 200 days of age, whereas the body weight of WT mice continued to increase (Fig. 6A). As expected, male and female WT mice on HFD were heavier than WT mice on CD and continued to gain weight throughout the duration of the study. Het mice on HFD were heavier than Het mice on CD but lighter than WT on HFD, indicating that HFD Het mice do not accumulate as much body fat as WT and maintain a body weight similar to WT on CD. Next, to characterize the body mass composition of the mice we performed echo-MRI in male mice at 250 days of age. For these studies, we used a cohort of symptomatic male mice (and aged matched WT male mice) to avoid confounding effects of hormonal cycling in female mice. Total body mass was increased in both Het and WT mice on HFD compared to CD (Fig. 6B). In both groups, HFD caused an increase of fat mass and a decrease of lean mass (Fig. 6C), suggesting that Het and WT mice on HFD underwent similar changes in body mass composition.

Metabolic cage studies were performed in male mice at 250 days of age. Total energy expenditure in light and dark cycles was not affected by genotype or diet (Supplementary Fig. 3A). Respiratory exchange ratio (RER, i.e., the ratio between VCO_2 and VO_2) showed significantly higher values in Het mice compared to WT mice on CD. This difference was significant both in the light and the dark, but more pronounced in the dark (Fig. 6D, E), and indicated that energy

metabolism in Het mice uses carbohydrate oxidation more than in WT animals. RER of Het mice in HFD was significantly lower than in CD, both in the light and in the dark, suggesting a shift towards FAO for energy metabolism. Interestingly, in the dark, when mice are awake and consume food, RER increases in both Het and WT on CD, but significantly more in the Het mice (Fig. 6D, E). Conversely, mice on HFD do not show changes in RER in the dark indicating absence of metabolic flexibility. Food intake in the light was not affected by genotype or diet (Fig. 6F), but significantly increased in Het mice on CD in the dark, an increase that was completely abolished in HFD.

Notably, when a running wheel was placed in the cage to allow for voluntary exercise, Het mice on CD ran on the wheel significantly more than WT in the dark (Fig. 6G). Instead, the distance traveled outside of the wheel in the dark was unchanged in WT and Het mice on CD (Supplementary Fig. 3B). Traveled distance in an open field test also confirmed that overall, WT and Het mice do not differ in total activity (Supplementary Fig. 3C). In HFD, both Het and WT mice ran significantly less in the dark than mice in CD, and differences between genotypes were abolished. These data showed that Het mice on CD display increased voluntary running on the wheel, which is eliminated by HFD. We examined the RER of mice allowed to run on the wheel. In the dark, the wheel increased the RER of WT mice on CD (Fig. 6H, I), indicating enhanced utilization of carbohydrates, while the RER of Het mice remained as high as without the wheel, presumably because the carbohydrate utilization was maximized, even without the wheel. Mice on HFD remained metabolically inflexible even in the presence of the wheel.

HFD is known to alter insulin sensitivity and decrease glucose uptake. To assess the effects of HFD on glucose uptake, we measured insulin sensitivity and glucose clearance capacity of these mice by insulin and glucose tolerance tests (ITT, GTT). While HFD did not significantly alter basal fasting glucose in either genotype relative to CD, baseline glucose levels were lower in HFD Het mice as compared to HFD WT (Fig. 7A). Insulin sensitivity (ITT) was decreased by HFD in both WT and Het mice, as shown by the lack of decrease of blood glucose after insulin administration (Fig. 7B). In the GTT, glucose clearance was similar in WT mice in HFD and CD (Fig. 7C). In Het mice, the glucose curve had higher amplitude and larger area under the curve compared to WT (Fig. 7D), but significantly more in HFD compared to CD. These results suggest that Het mice are less sensitive to insulin even in CD and show that HFD causes altered response to glucose load in both genotypes, but more significantly in Het mice.

Next, we analyzed the effects of HFD on liver enzymes in blood to assess on WT and Het mice at 250 days of age. Alkaline phosphatase (ALP), aspartate transaminase (AST), and alanine transaminase (ALT) were unaffected by genotype and diet (Supplementary Fig. 4A). Interestingly,

the albumin/globulin ratio was decreased by HFD in WT, but not in Het mice (Fig. 7E). Lactate dehydrogenase (LDH) was higher in WT HFD, but not in Het mice (Fig. 6F). Other blood chemistry parameters, including bilirubin, total protein, cholesterol, and triglycerides, were unchanged in both genotypes (Supplementary Fig. 4B-D).

Mice were sacrificed at 250 days of age to assess pathological changes. Liver hematoxylin-eosin staining highlighted vacuoles compatible with hepatic steatosis in WT HFD. Liver vacuolization was less abundant in Het HFD (Fig. 7G). Together, these results suggest that HFD caused hepatic alteration in WT, but not in Het mice, likely because Het mice do not accumulate as much fat as WT mice exposed to HFD. In the heart, Masson's trichrome staining indicated abundant fibrosis in Het mice on CD, whereas in HFD the Het heart showed vacuoles compatible with fat deposition, but less fibrosis (Fig. 7H).

Lastly, to investigate the systemic effects of HFD in WT and Het mice and identify potential circulating biomarkers, we performed serum metabolomic and lipidomic analyses at 250 days of age. In CD, there were only a small number of significantly different serum metabolites between WT and Het mice (Supplementary Fig. 5A), which did not define any apparent pathway. Surprisingly, HFD modified the serum levels of fewer metabolites in Het (Supplementary Fig. 5B,D) than in WT mice (Supplementary Fig. 5C,D). Furthermore, differentially abundant serum metabolites in HFD were largely non-overlapping in WT and Het mice (Supplementary Fig. 5D). Among the metabolites altered in Het mice, 9-Hydroxyoctadecadienoic acid (9-HODE) showed the highest statistical significance and high fold change (Supplementary Fig. 5B). 9-HODE is an oxidation product of linoleic acid, which is increased by oxidative stress (Vangaveti *et al*, 2010). This metabolite was not significantly different between Het and WT mice in CD, suggesting that it could serve a potential biomarker to monitor the effect of HFD in Het mice. Serum lipidomics analyses showed several species of lipids that were differentially represented based on genotype and diet (Supplementary Fig. 5E). The effects of HFD on serum lipids were partially overlapping between Het and WT mice (Supplementary Fig. 5F). However, there were several lipids, including phospholipids, sphingomyelins, and triglycerides that responded differentially in the two genotypes. Free fatty acids were also affected by HDF in both genotypes, as expected, but there were more significantly increased fatty acids in the serum of Het than WT mice (Supplementary Fig. 5G).

<u>HFD decreases CHCHD10 protein levels and aggregation in Het hearts</u>

Metabolic studies in Het mice showed that HFD induces a rearrangement in metabolism that enhances FAO at the expenses of glucose utilization. This rearrangement was associated with a

decrease of cardiomyopathy markers. To further understand the mechanism underlying these cardioprotective effects, we wanted to know if HFD also affected CHCHD10 at the protein level. To answer this question, we analyzed the steady state amounts of CHCHD10 in heart at 75 days of age. Western blot of tissue homogenates showed that HFD decreased the amount of CHCHD10 normalized by the mitochondrial protein Tim23 in Het hearts, but not in WT hearts (Fig. 8A,B). Moreover, filter trap assays of mitochondria isolated from heart showed a decrease in the amounts of insoluble CHCHD10 protein aggregates (Fig. 8C,D). Quantification of CHCHD10 gene expression by qPCR normalized by actin, however, showed no difference between Het hearts in CD and HFD (Fig. 8E), indicating that the decrease in CHCHD10 protein was not due to transcriptional changes in HFD. Together, these results indicate that HFD decreases the accumulation and aggregation of CHCHD10 in Het mice. Since HFD did not affect the levels of CHCHD10 in WT mice and did not change the transcription of CHCHD10 gene, we hypothesized that it may enhance the clearance of the aggregated protein or even of whole CHCHD10 aggregate containing mitochondria. Therefore, we examined the expression of a set of genes proposed to be involved in autophagy (Bordi *et al*, 2021). Some key autosomal induction genes such as *Atg7* and *Bcl2* (Fig. 8F) were downregulated in Het hearts on CD, while Het HFD hearts were significantly increased in Het HFD hearts. These findings suggest that autophagy may be induced by HFD in Het hearts. We then examined the levels of long vs. short forms of OPA1, whose ratio is known to be decreased in CHCHD10 mutant hearts (Liu *et al.*, 2020; Shammas *et al.*, 2022). We confirmed a trend suggestive of OPA1 cleavage in Het heart mitochondria under CD, which was unchanged by HFD (Fig. 8G,H). We also assessed the levels of SQSTM1 (p62) associated with mitochondria and confirmed its increase in Het hearts, as previously reported (Anderson *et al.*, 2019), which was decreased by HFD although it did not reach statistical significance ($p = 0.08$) (Fig. 8I,J). We also evaluated the levels of parkin in heart mitochondrial fractions. Parkin was significantly increased in Het CD relative to WT CD, while Het HFD had parkin levels comparable to WT CD (Fig 8K,L). Overall, these data suggests that HFD modulates the autophagic activity in Het hearts, possibly contributing to the decrease in CHCHD10 accumulation.

<u>HFD is cardioprotective during pregnancy</u>

Next, we wanted to assess if HFD treatment starting in adult life could be protective in Het mice. To this end, we took advantage of the accelerated mortality associated with the cardiac failure observed in pregnant Het female mice (Anderson *et al.*, 2019). Mating started at 65 days of age and continued until all female mice were dead. HFD started concomitantly with breeding.

Het female mice on CD and HFD had similar litter sizes at the first pregnancy (Fig. 9A). However, Het mice on HFD could survive more pregnancies on average (3.75 vs. 2.75, Fig. 9B). Strikingly, Het females on HFD, despite going through a higher number of pregnancies, survived much longer than those on CD (406.1 ± 36.9 days and 230.5 ± 49.5 days, respectively, Fig. 9C,D). Interestingly, Het female mice undergoing pregnancy on HFD lived even longer than the average lifespan of naïve females on a normal chow that we had reported previously (Fig. 9E, 350 days (Anderson *et al.*, 2019)). Heart size of Het females sacrificed within twenty-four hours after delivery of their first litter was slightly smaller in Het females on HFD, as compared to those on CD (Fig. 9F), and gene expression of cardiomyopathy markers (*Nppb* and *Myh6*) were reduced by the HFD as compared to CD although values did not reach statistical significance (Fig. 9G).

HFD protected the hearts of Het mice exposed to cardiac stress exacerbated by pregnancy. We wanted to determine if HFD could be protective in an independent mouse model of mitochondrial cardiomyopathy. To this end, we evaluated the effects of HFD on the disease course of a conditional heart frataxin (FXN) exon-2 KO mouse ($Fxn^{flox/null}$::MCK-Cre). This mouse model develops a rapidly progressing cardiomyopathy with weight loss and death at approximately 80 days of age, like a similar mouse model of cardiac FXN exon-4 KO (Puccio *et al*, 2001). Both males and female mice were treated with HFD or CD starting at 30 days of age. Surprisingly, HFD caused a small but significant decrease of body weight in both sexes (Supplementary Fig. 6A). HFD did not modify the lifespan of male mice, but increased the survival of females compared to CD (91.5 ± 3.7 days vs. 81.5 ± 3.7 days, respectively, Supplementary Fig. 6B,C). This result suggests that HFD cardio protection is context dependent and does not equally extend to all mouse models of mitochondrial cardiomyopathy.

Discussion

Mitochondrial proteotoxic stress causes the activation of the protease OMA1 resulting in OPA1 cleavage and remodeling of cristae structure. it also activates ISR through regulation of ATF4 translation by cleavage and cytosolic translocation of DELE1, another target of OMA1 (Fessler *et al*, 2020; Guo *et al*, 2020). This phenomenon was recently reported as being protective in different models of mitochondrial cardiomyopathy, such as CHCHD10 mutations (Shammas *et al.*, 2022) and cytochrome c oxidase deficiency (Ahola *et al*, 2022). In parallel, and potentially independent of OMA1 cleavage, mitochondrial stress also causes extensive metabolic rewiring (Kuhl *et al*, 2017; Shammas *et al.*, 2022). Metabolic rewiring in these models of mitochondrial cardiomyopathy included enhanced 1C metabolism and a preferential usage of glucose over fatty acids for energy production. The latter reminiscent of the energy metabolism of the fetal heart,

which is often described in situations of cardiac stress (Ritterhoff & Tian, 2017). We had previously proposed that in mutant CHCHD10 hearts this metabolic shift plays a pathological role (Sayles *et al.*, 2022). Findings from a mitochondrial cardiomyopathy associated with heart specific deletion of the protease YME1L suggested that forcing mutant cardiomyocytes to use FAO, by exposing mice to chronic HFD resulting in insulin resistance, has beneficial effects (Wai *et al.*, 2015). Therefore, in this study, we investigated the hypothesis that HFD could exert a protective role in the cardiomyopathy associated with mutant CHCHD10.

The effects of HFD differ significantly between WT and CHCHD10 mutant animals. Contrary to WT mice, Het mice did not become obese, even over a very long treatment that started in utero and continued for a year after weaning. Het mice did not develop liver steatosis or alterations of hepatic function typically associated with HFD in WT animals. As expected, HFD caused a decrease in RER in both WT and Het mice, consistent with increased FAO and decreased carbohydrate usage. However, extensive transcriptomics and metabolomics studies of the heart evidenced profound differences in response to HFD in WT and Het mice. Most importantly, pathways indicative of cardiac stress and cardiomyopathy markers were downregulated only in Het mice, supporting the cardioprotective effects of HFD in mitochondrial cardiomyopathy. To assess the translational value of this observation, we tested the effects of HFD in a model of severe cardiomyopathy induced by pregnancy in the female Het mice. In this case, HFD was initiated in adult life, at the time of breeding, and resulted in a striking extension of the lifespan of these Het animals.

Taken together, the findings from this study demonstrate that the metabolic changes induced by HFD differ substantially between control mice and mice affected by a primary mitochondrial disease, and that beneficial effects on the heart are confined to the latter. However, the benefits of HFD in mitochondrial cardiomyopathy models are context dependent. Mice with conditional deletion of FXN in heart and skeletal muscle develop a severe fatal mitochondrial cardiomyopathy (Puccio *et al.*, 2001), but HFD fails to extend the survival of cardiac-specific FXN KO male mice and only had a small, albeit statistically significant, life extension effect in females. Although these findings indicate an interesting sexual dimorphism in the response to HFD in the FXN, which deserves further investigation, they also demonstrate context-dependency for the protective effect of HFD. The reasons for this major difference in cardioprotection between mutant CHCHD10 and FXN KO mice likely lie on the mechanisms underpinning the mitochondrial stress. The loss of FXN causes FeS cluster assembly defects that compromise several enzymes necessary for oxidative phosphorylation (Rotig *et al*, 1997). Since FAO requires a viable oxidative phosphorylation machinery, it cannot be reactivated in FXN knock out hearts. On the other hand,

the cause of stress in mutant CHCHD10 mice is proteotoxic in nature and the oxidative phosphorylation function is largely preserved until disease end stage (Anderson *et al.*, 2019; Sayles *et al.*, 2022), thereby allowing for reactivation of FAO by HFD.

Lipidomics studies highlighted phospholipid alterations in the Het hearts relative to WT in CD. These differences had not been described before in CHCHD10 mutant mice and are of potential disease relevance because phospholipids play major structural and signaling roles that may affect mitochondria directly (Funai *et al*, 2020). A generalized decrease in several classes of phospholipids was evident, but especially interesting was the alteration of CL levels in the Het heart, since CL is a fundamental component of the mitochondrial inner membrane. Interestingly, aberrant mitochondrial cristae structure has been described in *in vivo* and *in vitro* models of pathogenic CHCHD10 mutations (Genin *et al.*, 2022), which could be at least in part due to CL abnormalities. In HFD, a subset of phospholipids in the Het hearts become more similar in abundance to WT hearts, suggesting that the normalization of the profiles of this class of lipids may participate in the cardioprotection afforded by HFD. In serum, the differences in lipid content between Het and WT mice were not as well delineated as in heart in CD, but upon HFD treatment differences in the levels of several phospholipids as well as triglycerides became evident, suggesting changes induced by mutant CHCHD10 in the response to HFD at the systemic level could involve several tissues, including the adipose tissue and liver. Intriguingly, in mice CHCHD10 has been implicated in mitochondrion-dependent browning of adipocytes (Xia *et al*, 2022) and lipolysis associated with thermogenesis (Ding *et al*, 2022).

We explored the transcriptomics and metabolomics profiles of Het and WT mice in the spinal cord, a region of the CNS pathologically affected by CHCHD10 mutations manifesting with ALS symptoms (Keith *et al*, 2020). In Het mice, the spinal cord displays CHCHD10 aggregation and motor neuron mitochondrial structural abnormalities (Anderson *et al.*, 2019). Surprisingly, we did not detect significant alterations of the transcriptional profiles in the spinal cord of Het mice in CD and minimal effects of HFD. This could be due to the potentially cell specific nature of the pathology, which may be undetectable by bulk tissue transcriptomics. Single cell or nuclei sequencing could in the future be employed to analyze specific cell types, such as motor neurons. Additionally, it is possible that changes in spinal cord transcriptomic profiles only arise later in the course of the disease in this mouse model. The modest effect of HFD on the spinal cord transcriptomics could be explained by limited utilization of fatty acids as energy substrate in the CNS. We interpret the differences in metabolites detected in the spinal cord as the result of systemic effects, with molecules transported across the blood brain barrier, rather than effects of changes in spinal cord metabolism. The phenotypic alterations in neurological functions in Het

mice exposed to HFD were also limited, as these animals do not show clear neurological symptoms until late in the disease (Anderson *et al.*, 2019; Genin *et al.*, 2019). Nevertheless, in this study we observed a hyperactivity phenotype, which had not been previously described, manifesting with increased voluntary running on the wheel in the Het mice. Although the mechanisms remain to be elucidated, HFD completely eliminated this hyperactivity phenotype in Het mice.

We did not expect that HFD would decrease the mitochondrial stress induced by mutant CHCHD10 in the heart. In fact, several markers of mitochondrial stress persisted in Het hearts in HFD, including increased OPA1 cleavage and p62 accumulation on mitochondria. However, we were surprised to find decreased steady state levels of CHCHD10 protein in heart mitochondria of HFD treated Het mice and decreased amounts of insoluble, aggregated CHCHD10 in the filter trap experiments. One potential explanation is that the turnover of aggregated CHCHD10 is increased in the mutant heart exposed to HFD. Some of the RNA markers of autophagy that were downregulated in Het in CD, were increased by HFD, including *Atg7,* which could result in enhanced turnover of mitochondria that have accumulated aggregated CHCHD10. In support of this interpretation, HFD was shown to increase mitophagy in a mouse model of diabetic cardiomyopathy, where general autophagy was upregulated for up to 8 weeks of HFD and then it decreased, while an enhancement of mitophagy persisted throughout the duration of the chronic HFD treatment (Tong *et al*, 2019). At the same time, RNA markers of mitochondrial biogenesis, such as PGC1α, were elevated in Het mice on HFD, suggesting that increased mitochondrial autophagy could be balanced by enhanced mitochondrial biogenesis, thereby improving mitochondrial homeostasis. This hypothesis will need to be further explored in the future, by investigating autophagy and mitophagy fluxes, as well as mitochondrial biogenesis, in Het and wild type hearts in CD and HFD.

Overall, the positive outcome of HFD treatment in the CHCHD10 mouse model suggest a path forward towards metabolic therapy approaches for certain forms of mitochondrial diseases, but there are limitations that will need to be addressed experimentally in future work. In this study, we opted to treat mice since gestation to maximize the duration and impact of HFD and only initiated the treatment in adults for the pregnant female paradigm. In the future, it will be necessary to investigate the effects of HFD also in adult males. We did not perform survival studies in the mice treated since gestation, because this type of treatment is not clinically relevant, as human patients would likely be treated after diagnosis. Furthermore, it is possible that, as the disease worsen in older animals, the effects of HFD may wane because mitochondrial damage starts impairing oxidative phosphorylation (Anderson *et al.*, 2019) and the heart can no longer use FAO efficiently.

Therefore, the effects of HFD initiated at disease onset and continued until end stage will have to be tested. Importantly, the molecular mechanisms underlying the decrease of aggregated CHCHD10 in heart mitochondria of HFD treated Hets and the role of these mechanisms as disease modifier will have to be further explored.

The finding of cardioprotection by HFD in a mouse model of mitochondrial cardiomyopathy associated with protein aggregation and mtISR suggests potential therapeutic avenues to be explored in human patients. However, the translatability of these findings to humans affected by CHCHD10 remain to be determined. Potentially, a HFD strategy could be employed in the pedigrees with CHCHD10 mutations that present with cardiomyopathy (Shammas *et al.*, 2022), whereas it is uncertain whether HFD could have beneficial effects in patients with predominantly neurological manifestations. On the other hand, HFD could be considered as a therapeutic approach in other forms of mitochondrial cardiomyopathy caused by similar pathogenic mechanisms, as long as the oxidative phosphorylation machinery is preserved. HFD has traditionally been considered a modeling tool to elicit metabolic syndrome and its pathological consequences in experimental animals. However, we propose that in the case of CHCHD10 cardiomyopathy, and possibly other similar disorders, HFD has fewer detrimental effects, because of the underlying metabolic conditions. This notion is supported by the observation that HFD, does not cause overt obesity and hepatic alterations in Het mice. Nevertheless, alternative pharmacological strategies to enhance FAO and decrease glucose utilization in mitochondrial cardiomyopathies could be developed in the future and potentially used in conjunction with other therapeutic approaches.

Methods

Animals

All animal procedures were conducted in accordance with Weill Cornell Medicine (WCM) Animal Care and Use Committee and performed according to the Guidelines for the Care and Use of Laboratory Animals of the National Institutes of Health. CHCHD10^{S55L} knock-in mice were previously generated by CRISPR/Cas9 approach (Anderson *et al.*, 2019) and are available as Stock #028952 from the Jackson Laboratory. Breeding was set up between CHCHD10^{S55L} heterozygous (het) males with wildtype (WT) C57BL/6NJ females (Jackson Laboratory, stock #005304). Tail DNA was extracted with a Promega kit and genotype was determined by sequencing services at Transnetyx. Conditional heart frataxin (FXN) exon-2 KO mice (Fxn$^{flox/null}$::MCK-Cre) were purchased from Jackson Laboratory (stock #029720).

High fat diet treatment

High fat diet (HFD) containing 60% fat, 20% protein, 20% carbohydrates (D12492) and the calorie and sucrose matched control diet (CD; D12450J) were purchased from Research Diets (New Brunswick, NJ). For the pregnancy paradigm, het females (P65) were mated with WT males and fed the HFD or CD for the mating/survival period until death. Offspring from the mating pairs were continued on the respective diet until adulthood. For FXN KO mice, treatment was started at 4 weeks of age.

Serum collection

Blood was collected by cheek bleeds into serum separator tubes. Serum was separated after 30 minutes of clotting at room temperature and centrifugation at 2000xg for 15 min. Serum liver enzymes were assessed at the Comparative Pathology Core at Memorial Sloan Kettering Cancer Center.

Behavioral assays

Body weight was measured biweekly starting at weaning. For survival analyses, the age of death or the age at which institutional guidelines required euthanasia was recorded for the Kaplan-Meier survival curve.

Metabolic phenotyping

Metabolic rate of Het and WT male mice was assessed in real time in the temperature and light-controlled Promethion High-definition Multiplexed Respirometry System at the WCM Metabolic Phenotyping Center. Food and water intake, and body mass are assessed gravimetrically. Distance traveled (activity) is determined by the XY position displacements represented by beam breaks. 24 hour recordings were measured with and without a running wheel. Energy expenditure is determined from indirect calorimetry and calculated by the Weir equation, and RER is calculated as $VCO_2/V\ O_2$. Body composition, including total body, fat, and lean mass, as well as free and total water, in each mouse was measured by Echo-MRI.

Intraperitoneal glucose tolerance test (IP-GTT)

Mice are fasted for 18 hours prior to glucose injection. A bolus of 2 g/kg glucose was administered by intraperitoneal injection (IP). Tail vein blood were drawn at 15 min intervals from 0-120 min to assess glucose levels by a blood glucose meter.

Intraperitoneal insulin tolerance test (IP-ITT)

Mice are fasted for 6 hours prior to insulin injection. A bolus of 0.5 U/kg insulin was administered by IP. Tail vein blood were drawn at 15 min intervals from 0-90 min to assess glucose levels.

Liver and heart pathology

Pathological analyses of the liver and heart were performed by the Laboratory of Comparative Pathology at Memorial Sloan Kettering Cancer Center. Female mice (aged P250-300) were sacrificed by cervical dislocation, tissues were harvested and fixed in 10% buffered formalin for 48 hours. Liver and heart were processed and embedded in paraffin. Sections were cut at a thickness of 5 µm and stained with hematoxylin and eosin (H&E). Masson's trichrome stain was performed to assess collagen content in the heart. Necropsy and histopathology evaluation was performed by a board-certified veterinary pathologist.

Western Blotting

Mitochondrial-enriched fractions were isolated from heart tissue by differential centrifugation (Gostimskaya & Galkin, 2010). Protein concentration was determined by the Bradford protein assay (Bio-Rad). Mitochondrial (5 µg) fractions were denatured in 1X Laemmli Buffer (Bio-Rad) containing 2-Mercaptoethanol at 95°C for 10 min and separated by electrophoresis in a 4–12% SDS–PAGE gel (Bio-Rad) and transferred to a PVDF membrane (Bio-Rad). For the Opa1 blot, a 4-12% NuPAGE gel (Thermo Fisher) with the MOPS running buffer was used for electrophoresis. Blots were incubated in 3% BSA in TBS with 1% Tween-20 (TBST) for one hour at room temperature. Primary antibodies were incubated overnight at 4°C. Secondary antibodies were incubated for 45 min at room temperature. In all blots, proteins were detected using Clarity Western ECL Blotting Substrates (Bio-Rad) and imaged on ChemiDoc Touch (Bio-Rad). The antibodies used are anti-CHCHD10 (Sigma, HPA003440) anti-p62/SQSTM1 (Novus, H00008878-M01), anti-Parkin (Santa Cruz, SC32282), and anti-OPA1 (BD Transduction Lab, 612606).

Filter Trap Assay

Insoluble protein aggregates were detected by filter trap assay as previously described (Palomo *et al*, 2018). Briefly, 5 µg of mitochondrial fractions were solubilized with 1% NP-40 in PBS for 15 min on ice. Samples were loaded onto a Bio-Dot Microfiltration apparatus (Bio-Rad) containing a cellulose acetate membrane (0.2 µm pore diameter, Whatman). Vacuum was applied to pass samples through the membrane, which was then was washed with 1% Tween-20 in PBS. Trapped

proteins were detected with anti-CHCHD10 antibody (Sigma, 1:500) followed by secondary antibody (anti-Rb). Blots were then imaged on the ChemiDoc Touch.

3'-RNA seq

RNA was extracted from heart and spinal cord using TRIzol (ThermoFisher) and the SV Total RNA Isolation System (Promega). 3'RNAseq libraries were prepared from 500 ng of RNA per sample using the Lexogen QuantSeq 3' mRNA-Seq Library Prep Kit FWD for Illumina and pooled for reduced run variability. Libraries were sequenced with single-end 86 bps on an Illumina NextSeq500 sequencer (Cornell BRC Facility). Raw sequence reads were processed using the BBDuk program in the BBMap package. Trimmed reads were aligned to the mouse genome assembly GRCm38.p6 using the STAR aligner (version 2.5.0a). SAM files were converted to BAM to read overlapping reads per gene using HTSeq-count (version 0.6.1). Gene expression profiles were constructed for differential expression, cluster, and principal component analyses with the R package DESeq2 (Anders *et al*, 2015). For normalization and differential gene expression analysis, a low counts filter of <96 was used and all other filtering parameters were kept as defaults. A Wald test was used to determine statistical significance, with the cutoff being a False Discovery Rate <5% after Benjamini-Hochberg correction. Pathway analysis for all gene expression data was performed with the gprofiler2 (Kolberg *et al*, 2020) and clusterProfiler packages (Wu *et al*, 2021), using the gene ontology (GO) Molecular Function (GO:MF), GO Biological Process (GO:BP), and Kyoto Encyclopedia of Genes and Genomes (KEGG) databases. Cutoff for significance was FDR corrected p-value < 0.05. Pathways shown in the figures were condensed using the simplify function from the clusterProfiler package (Wu *et al.*, 2021) to merge terms with more than 40% overlapping annotated genes.

Untargeted polar metabolomic profiling

15 mg of cardiac tissue was homogenized in 80% methanol (Sigma) using Tissue Tearer (BioSpec) on dry ice. Samples were incubated at -80ºC for 4 hours. Homogenates were then centrifuged at 14,000 rfc for 20 min at 4ºC. The supernatant was extracted and stored at -80ºC. The Weill Cornell Medicine Meyer Cancer Center Proteomics & Metabolomics Core Facility performed hydrophilic interaction liquid chromatography-mass spectrometry (LC-MS) for relative quantification of targeted polar metabolite profiles. Metabolites were measured on a Q Exactive Orbitrap mass spectrometer, coupled to a Vanquish UPLC system by an Ion Max ion source with a HESI II probe (Thermo Scientific). A Sequant ZIC-pHILIC column (2.1 mm i.d. × 150 mm, particle size of 5 µm, Millipore Sigma) was used for separation. The MS data was processed using

XCalibur 4.1 (Thermo Scientific) to obtain the metabolite signal intensity for relative quantitation. Targeted identification was available for 205 metabolites based on an in-house library established using known chemical standards. Identification required exact mass (within 5ppm) and standard retention times. Peak intensities for metabolites were screened for missing values and relative metabolite abundance data was analyzed by using MetaboAnalyst software version 5.0 (Pang *et al*, 2021). Metabolite significance was determined with one-way ANOVA with post-hoc t-tests, with the cutoff being a raw p-value <0.05, and the pathway significance cutoff was FDR corrected p-value <0.05.

Lipidomics

Lipids were extracted from samples as previously described (Satomi *et al*, 2017). In brief, 1 ml or 180 µl of 90% isopropanol was added to 15 mg of homogenized heart tissue or 20 µl serum, respectively. Samples were vortexed for 2 min, sonicated for 1 min using a probe sonicator and centrifuged at 15,000 g for 10 min. The supernatant was collected and dried down using a SpeedVac. The dried samples were reconstituted using acetonitrile/isopropanol/water 65:30:5 containing stable isotope labeled internal lipid standards (Splash Lipidomix, Avanti Polar Lipids) prior to LC-MS analysis.

Chromatographic separation was performed on a Vanquish UHPLC system with a Cadenza CD-C18 3 µm packing column (Imtakt, 2.1 mm id x 150 mm) coupled to a Q Exactive Orbitrap mass spectrometer (Thermo Scientific) via an Ion Max ion source with a HESI II probe (Thermo Scientific). The mobile phase consisted of buffer A: 60% acetonitrile, 40% water, 10 mM ammonium formate with 0.1% formic acid and buffer B: 90% isopropanol, 10% acetonitrile, 10 mM ammonium formate with 0.1% formic acid. The LC gradient was as follows: 0–1.5 min, 32% buffer B; 1.5-4 min, 32-45% buffer B; 4-5 min, 45-52% buffer B; 5-8 min, 52-58% buffer B; 8-11 min, 58-66% buffer B; 11-14 min, 66-70% buffer B; 14-18 min, 70-75% buffer B; 21-25 min, isocratic 97% buffer B, 25-25.1 min 97-32% buffer B; followed by 5 min of re-equilibration of the column before the next run. The flow rate was 200 µl/min. A data-dependent mass spectrometric acquisition method was used for lipid identification. In this method, each MS survey scan was followed by up to 10 MS/MS scans performed on the most abundant ions. Data was acquired in positive and negative mode in separate runs. The following electrospray parameters were used: spray voltage 3.0 kV, heated capillary temperature 350 °C, HESI probe temperature 350 °C, sheath gas, 35 units; auxiliary gas 10 units. For MS scans: resolution, 70,000 (at m/z 200); automatic gain control target, 3e6; maximum injection time, 200 ms; scan range, 250-1800 m/z.

For MS/MS scans: resolution, 17,500 (at 200 m/z); automatic gain control target, 1e5 ions; maximum injection time, 75 ms; isolation window, 1 m/z; NCE, stepped 20,30 and 40.
The LC-MS results were processed using MS-DIAL software (version 4.9) for lipid identification and relative quantitation.

Free Fatty Acid Analyses

Free fatty acids were extracted from serum using 90% methanol (LC/MS grade, Thermo Scientific). The extracts were clarified by centrifugation at 15,000 g for 10 min. The supernatant was collected and dried down using a SpeedVac. The dried sample was reconstituted using 50% methanol prior to LC-MS analysis.
Chromatographic separation was performed on a Vanquish UHPLC system (Thermo Scientific) with a Cadenza CD-C18 3 µm packing column (Imtakt, 2.1 mm id x 150 mm) coupled to a Q Exactive Orbitrap mass spectrometer (Thermo Scientific) via an Ion Max ion source with a HESI II probe (Thermo Scientific). The mobile phase consisted of buffer A: 5 mM ammonium acetate in water (LC/MS grade, Thermo Scientific) and buffer B: 5 mM ammonium acetate, 85% isopropanol (LC/MS grade, Thermo Scientific), 10% acetonitrile (LC/MS grade, Thermo Scientific), and 5% water. The LC gradient was as follows: 0–1.5 min, 50% buffer B; 1.5-3 min, 50-90% buffer B; 3-5.5 min, 90-95% buffer B; 5.5-10 min, 95% buffer B, followed by 5 min of re-equilibration of the column before the next run. The flow rate was 150 µL/min. MS data was acquired in negative mode. The following electrospray parameters were used: spray voltage 3.0 kV, heated capillary temperature 350 °C, HESI probe temperature 350 °C,sheath gas, 35 units; auxiliary gas 10 units. For MS scans: mass scan range, 140-1000 m/z; resolution, 70,000 (at m/z 200); automatic gain control target, 1e6; maximum injection time, 50 ms.
MS data files were processed using XCalibur (version 4.1, Thermo Scientific). Identification of free fatty acids was based on accurate masses within 5 ppm and standard retention times from compound standards. Relative quantitation was performed based on MS signal intensities.

Statistical Analyses

Data visualization was done in R using the ggplot2, Enhanced volcano plot, and Venn diagram packages available from CRAN, and in GraphPad Prism version 9.3 (GraphPad Software, Inc). All numerical data are expressed as mean ± standard deviation. Statistical comparisons were made in GraphPad Prism. For metabolite comparisons, ANOVA with Brown Forsythe and Welch's correction was used. * $p < 0.05$, ** $p < 0.01$, *** $p < 0.0005$, **** $p < 0.0001$. For differential gene expression analyses, Two-tail unpaired student's t-tests were used for sample comparisons.

Corrected p values were calculated based on the Benjamini–Hochberg method to adjust for multiple comparisons. For survival studies, data were analyzed by Kaplan-Meir curve and Mantel-Cox log rank test. Biological replicate information for each experiment, as well as number of mice, age, and sex, are indicated in the figure legends.

Acknowledgements

We thank the Weill Cornell Medicine Proteomics & Metabolomics Core Facility, Metabolic Phenotyping Core, Comparative Pathology Core at Memorial Sloan Kettering Cancer Center, and the Cornell BRC Genomics Facility for their contributions. Schematics were created with BioRender.com.

Funding

NextGenALS 2021-01 to HK and GM, Muscular Dystrophy Association (MDA) 961871-01 to HK, NIH/NINDS R35 NS122209 to GM, MDA602894 to GM, NIH/NINDS NS122209-02S1 to NS.

Figure Legends

Figure 1. A, Volcano plot of heart DEGs between Het and WT mice on CD. Threshold set at FC 2 and p adjusted < 0.05. B, Volcano plot of heart DEGs between Het HFD vs. Het CD. C, Volcano plot of heart DEGs between WT HFD vs. WT CD. D, Volcano plot of heart DEGs between Het HFD vs. WT CD. E, Dot plot of pathway enrichment of all upregulated DEGs (padj <0.05) between Het CD vs. WT CD in heart. F, Dot plot of overrepresented pathways with downregulated DEGs between Het HFD and Het CD hearts. G, Heatmap showing effect of HFD on genes identified in the stress induced cardiac hypertrophy pathway. Asterisks denotes significantly different genes (padj <0.05).

Figure 2. A, Volcano plot showing differential abundance of heart metabolites from Het and WT mice on CD. Threshold set at FC 1 and p < 0.05. B, Differential abundance of heart metabolites between Het HFD vs. Het CD. C, Volcano plot with differential abundance of heart metabolites from WT HFD vs. WT CD. D, Venn diagram of metabolites both up and down regulated by HFD within each genotype separately (Het HFD vs Het CD, WT HFD vs WT CD). E and F, Pathways that were upregulated (E) and downregulated (F) by HFD only in WT heart (WT HFD vs. WT CD). G and H, Upregulated (G) and downregulated (H) pathways only in the Het HFD vs. Het CD. I) Heatmap of top 50 differentially abundant metabolites in Het and WT heart on CD or HFD.

Figure 3. A, Scheme of FAO pathway. B, Heatmap of genes encoding enzymes of the FAO pathway. C, Heatmap of genes encoding for enzymes in the glycolytic pathway. D, Glycolytic metabolite content in heart. E, Scheme of 1 carbon metabolism pathway. F, Heatmap of genes for 1 carbon metabolism enzymes. G, Intermediate metabolite levels in the 1 carbon metabolism pathway in heart. H, Adenosine levels in the heart. Asterisks denotes significantly different genes (padj <0.05).

Figure 4. A, Heatmap of top 50 phospholipids in Het and WT heart on CD or HFD.
B, Venn diagram of lipids that were up and down regulated (p <0.05) by HFD within each genotype separately (Het HFD vs Het CD, WT HFD vs WT CD). C, Heatmap of cardiolipins in Het and WT heart on CD or HFD. D, Scheme of phospholipid biosynthesis. E, Heatmap of genes involved in phospholipid biosynthesis. Asterisks denotes significantly different genes (padj <0.05).

Figure 5. A, Volcano plot of spinal cord differentially abundant metabolites between Het and WT mice on CD. Threshold set at FC 1 and p < 0.05. B, Volcano plot of differentially abundant metabolites in spinal cord between Het HFD vs. Het CD. C, Volcano plot of differentially abundant metabolites between WT HFD vs. WT CD. D, Volcano plot of spinal cord differentially abundant metabolites between Het HFD vs. WT CD. E, Venn diagram of metabolites both up and down regulated by HFD (p<0.05) within each genotype separately (Het HFD vs Het CD, WT HFD vs WT CD). F, Overrepresented pathways upregulated by HFD only in the Het heart. G, Overrepresented pathways upregulated by HFD only in the WT heart. H, Overrepresented pathways by HFD commonly downregulated by HFD in both Het and WT.

Figure 6. A, Body weight progression in Het and WT mice on CD or HFD up to a year. n=10-12 females per group, n=8-13 males per group. B, Body mass of Het and WT male mice on CD or HFD at P250. n = 6 per group C, Body composition determined by echo-MRI in Het and WT male mice on CD or HFD at P250. D, Respiratory exchange ratio (RER) of Het and WT mice measured in the Promethion metabolic phenotyping cage over 24 hours (no wheel) and calculated as VCO_2/VO_2. n = 6 per group. E, Average RER quantified in the light and dark cycles in cage without wheel. F, Food intake during the light/dark cycles. Mice in cages without wheels. G, Distance traveled voluntarily on the wheel. H, RER over 24 hours while the mice were in cages with wheels. I, Average RER quantified in the light and dark cycles, in cages with wheel present.

Figure 7. A, Glucose levels in Het and WT mice on CD or HFD at P250, upon fasting for 18 hours. B, Upon addition of a bolus of insulin at time 0, clearance of blood glucose was monitored for 60 min. C, Blood glucose clearance is measured after a bolus of glucose is given to mice at time 0. D, Blood glucose content during the 90 min quantified as area under the glucose curves. E, Serum albumin to globulin ratio in Het and WT mice on CD or HFD at P250. F, Serum lactate dehydrogenase levels are high in WT mice on HFD. ** $p < 0.01$. G, Hematoxylin and eosin staining of liver of P250 mice. Steatosis is not evident in HFD mice. H, Heart fibrosis by Mason's trichrome stain was evident in Het mice, but HFD did not alter fibrosis in WT or Het hearts.

Figure 8. A, Representative western blot of CHCHD10 (D10) and mitochondrial inner membrane translocase (Tim23) in P75 heart of WT and Het mice. B, Quantification of CHCHD10 in heart of WT and Het mice, normalized to Tim23 for mitochondrial content. n = 3 per group. C, NP40 insoluble CHCHD10 aggregates trapped in nitrocellulose filter. Het heart on CD shows increased levels of insoluble CHCHD10 aggregates that are reduced in Het heart on HFD. D, Quantification of NP40 insoluble aggregates. n = 4 per group. E, *Chchd10* mRNA from P75 heart show no difference between genotype or diet effect. n = 4 per group. F, Heatmap of genes involved in the autophagy pathway. Asterisks denotes significantly different genes (padj <0.05). G, Representative western blot of Opa1. H, Long Opa1 to the proteolytically processed, short Opa1 ratio was quantified. n = 3 per group. I, Representative western blot of P62 in P75 heart, and Tim23. J, Quantification of P62. n = 6 per group. K. Representative western blot of Parkin and Tim23 in P75 heart. N = 3 per group.

Figure 9. A, Average number of pups born per litter from het female dams on CD or HFD were similar. B, Average number of pups reared till weaning was similar in the litters born. C, Kaplan-Meir survival curve plotting probability against number of pregnancies. N = 8 females per group. D, Kaplan-Meir survival curve shows significant effect of HFD of survival of Het females going through multiple pregnancies ($P < 0.0001$). E, Median age at death of Het females on CD or HFD. **** $p < 0.0001$ by unpaired t-test. F, The heart weight relative to tibia length of Het dams, immediately after giving birth. n= 5 per group. G, mRNA expression of cardiomyopathy markers *Nppb* and *Myh6* in Het HFD or CD heart after pregnancy. n = 5 per group.

Supplementary Figure 1. A, Heatmap of triglycerides in Het and WT heart on CD or HFD. B, Heatmap of cholesterol esters in Het and WT heart on CD or HFD show no difference in abundance due to genotype or diet.

Supplementary Figure 2. A, Volcano plot of spinal cord DEGs between Het and WT mice on CD. B, Volcano plot of DEGs between Het spinal cord on HFD and Het spinal cord on CD. C, Volcano plot of spinal cord DEGs between WT mice on HFD and WT mice on CD.

Supplementary Figure 3. A, Energy expenditure (EE) during the light and dark cycle of mice in the Promethion metabolic phenotyping cage without the wheels. The calculated energy expenditure was adjusted to total body mass. B, Distance traveled in the cage, off the wheel, when the wheel was present in the cage. n = 6 per group of males. C, Ambulatory distance in 30 minutes of recording in an open field test system. D, Ratio of ambulatory time spent in a specified zone of the recording cage (zone 1) to the remainder, and versus total ambulatory time. n = 3-10 mice per group.

Supplementary Figure 4. A, Serum Alkaline phosphatase (ALP), aspartate transaminase (AST), and alanine transaminase (ALT) levels indicating liver function in Het and WT mice on CD or HFD at P250. B, Serum cholesterol (CHOL) and triglyceride (TRIG) levels. C, Serum bilirubin contents were measured. Total bilirubin (TBIL), direct bilirubin (DBIL), indirect bilirubin (IBIL). D, Serum total protein content. n = 6 per group.

Supplementary Figure 5. A, Volcano plot of serum metabolites in Het CD and WT CD mice at P250. B, Volcano plot of serum metabolites in Het HFD and Het CD mice. C, Volcano plot of serum metabolites in WT HFD and WT CD mice, D, Venn diagram of serum metabolites both up and down regulated by HFD (raw $p<0.1$) within each genotype separately (Het HFD vs Het CD, WT HFD vs WT CD). E. Heatmap of top 50 metabolites (by interquartile range) in serum of Het and WT mice on CD or HFD. F, Venn diagram of serum lipids up or down regulated by HFD (raw $p<0.1$) within each genotype separately. G, Venn diagram of serum free fatty acids up or down regulated by HFD (raw $p<0.1$) within each genotype separately.

Supplementary Figure 6. A, Body weight of heart Frataxin knockout males and females on CD or HFD. *$p < 0.05$. B, Kaplan-Meir survival curve shows effect of HFD on female Frataxin knockout females. $P < 0.05$ by unpaired t-test. C, Median age at death of Frataxin knockout mice on CD or HFD. ** denotes $p < 0.05$ by unpaired t-test.

References

Ahola S, Rivera Mejias P, Hermans S, Chandragiri S, Giavalisco P, Nolte H, Langer T (2022) OMA1-mediated integrated stress response protects against ferroptosis in mitochondrial cardiomyopathy. *Cell Metab* 34: 1875-1891 e1877

Anders S, Pyl PT, Huber W (2015) HTSeq--a Python framework to work with high-throughput sequencing data. *Bioinformatics* 31: 166-169

Anderson CJ, Bredvik K, Burstein SR, Davis C, Meadows SM, Dash J, Case L, Milner TA, Kawamata H, Zuberi A *et al* (2019) ALS/FTD mutant CHCHD10 mice reveal a tissue-specific toxic gain-of-function and mitochondrial stress response. *Acta Neuropathol* 138: 103-121

Bannwarth S, Ait-El-Mkadem S, Chaussenot A, Genin EC, Lacas-Gervais S, Fragaki K, Berg-Alonso L, Kageyama Y, Serre V, Moore DG *et al* (2014) A mitochondrial origin for frontotemporal dementia and amyotrophic lateral sclerosis through CHCHD10 involvement. *Brain* 137: 2329-2345

Bordi M, De Cegli R, Testa B, Nixon RA, Ballabio A, Cecconi F (2021) A gene toolbox for monitoring autophagy transcription. *Cell Death Dis* 12: 1044

Burstein SR, Valsecchi F, Kawamata H, Bourens M, Zeng R, Zuberi A, Milner TA, Cloonan SM, Lutz C, Barrientos A *et al* (2018) In vitro and in vivo studies of the ALS-FTLD protein CHCHD10 reveal novel mitochondrial topology and protein interactions. *Hum Mol Genet* 27: 160-177

Chia R, Chio A, Traynor BJ (2018) Novel genes associated with amyotrophic lateral sclerosis: diagnostic and clinical implications. *Lancet Neurol* 17: 94-102

Ding M, Ma YJ, Du RQ, Zhou WY, Dou X, Yang QQ, Tang Y, Qian SW, Liu Y, Pan DN *et al* (2022) CHCHD10 Modulates Thermogenesis of Adipocytes by Regulating Lipolysis. *Diabetes* 71: 1862-1879

Fessler E, Eckl EM, Schmitt S, Mancilla IA, Meyer-Bender MF, Hanf M, Philippou-Massier J, Krebs S, Zischka H, Jae LT (2020) A pathway coordinated by DELE1 relays mitochondrial stress to the cytosol. *Nature* 579: 433-437

Funai K, Summers SA, Rutter J (2020) Reign in the membrane: How common lipids govern mitochondrial function. *Curr Opin Cell Biol* 63: 162-173

Genin EC, Bannwarth S, Lespinasse F, Ortega-Vila B, Fragaki K, Itoh K, Villa E, Lacas-Gervais S, Jokela M, Auranen M *et al* (2018) Loss of MICOS complex integrity and mitochondrial damage, but not TDP-43 mitochondrial localisation, are likely associated with severity of CHCHD10-related diseases. *Neurobiol Dis* 119: 159-171

Genin EC, Bannwarth S, Ropert B, Lespinasse F, Mauri-Crouzet A, Auge G, Fragaki K, Cochaud C, Donnarumma E, Lacas-Gervais S *et al* (2022) CHCHD10 and SLP2 control the stability of the PHB complex: a key factor for motor neuron viability. *Brain* 145: 3415-3430

Genin EC, Madji Hounoum B, Bannwarth S, Fragaki K, Lacas-Gervais S, Mauri-Crouzet A, Lespinasse F, Neveu J, Ropert B, Auge G *et al* (2019) Mitochondrial defect in muscle precedes neuromuscular junction degeneration and motor neuron death in CHCHD10(S59L/+) mouse. *Acta Neuropathol* 138: 123-145

Gostimskaya I, Galkin A (2010) Preparation of highly coupled rat heart mitochondria. *J Vis Exp*

Guo X, Aviles G, Liu Y, Tian R, Unger BA, Lin YT, Wiita AP, Xu K, Correia MA, Kampmann M (2020) Mitochondrial stress is relayed to the cytosol by an OMA1-DELE1-HRI pathway. *Nature* 579: 427-432

Johnson JO, Glynn SM, Gibbs JR, Nalls MA, Sabatelli M, Restagno G, Drory VE, Chio A, Rogaeva E, Traynor BJ (2014) Mutations in the CHCHD10 gene are a common cause of familial amyotrophic lateral sclerosis. *Brain* 137: e311

Keith JL, Swinkin E, Gao A, Alminawi S, Zhang M, McGoldrick P, McKeever P, Robertson J, Rogaeva E, Zinman L (2020) Neuropathologic description of CHCHD10 mutated amyotrophic lateral sclerosis. *Neurol Genet* 6: e394

Kitakaze M, Hori M (2000) Adenosine therapy: a new approach to chronic heart failure. *Expert Opin Investig Drugs* 9: 2519-2535

Kolberg L, Raudvere U, Kuzmin I, Vilo J, Peterson H (2020) gprofiler2 -- an R package for gene list functional enrichment analysis and namespace conversion toolset g:Profiler. *F1000Res* 9

Kuhl I, Miranda M, Atanassov I, Kuznetsova I, Hinze Y, Mourier A, Filipovska A, Larsson NG (2017) Transcriptomic and proteomic landscape of mitochondrial dysfunction reveals secondary coenzyme Q deficiency in mammals. *Elife* 6

Liu YT, Huang X, Nguyen D, Shammas MK, Wu BP, Dombi E, Springer DA, Poulton J, Sekine S, Narendra DP (2020) Loss of CHCHD2 and CHCHD10 activates OMA1 peptidase to disrupt mitochondrial cristae phenocopying patient mutations. *Hum Mol Genet* 29: 1547-1567

Muller K, Andersen PM, Hubers A, Marroquin N, Volk AE, Danzer KM, Meitinger T, Ludolph AC, Strom TM, Weishaupt JH (2014) Two novel mutations in conserved codons indicate that CHCHD10 is a gene associated with motor neuron disease. *Brain* 137: e309

Nguyen MK, McAvoy K, Liao SC, Doric Z, Lo I, Li H, Manfredi G, Nakamura K (2021) Mouse midbrain dopaminergic neurons survive loss of the PD-associated mitochondrial protein CHCHD2. *Hum Mol Genet*

Palomo GM, Granatiero V, Kawamata H, Konrad C, Kim M, Arreguin AJ, Zhao D, Milner TA, Manfredi G (2018) Parkin is a disease modifier in the mutant SOD1 mouse model of ALS. *EMBO Mol Med* 10

Pang Z, Chong J, Zhou G, de Lima Morais DA, Chang L, Barrette M, Gauthier C, Jacques P, Li S, Xia J (2021) MetaboAnalyst 5.0: narrowing the gap between raw spectra and functional insights. *Nucleic Acids Res* 49: W388-w396

Prasun P, LoPiccolo MK, Ginevic I (1993) Long-Chain Hydroxyacyl-CoA Dehydrogenase Deficiency / Trifunctional Protein Deficiency. In: *GeneReviews(®)*, Adam M.P., Everman D.B., Mirzaa G.M., Pagon R.A., Wallace S.E., Bean L.J.H., Gripp K.W., Amemiya A. (eds.)University of Washington, Seattle

Copyright © 1993-2023, University of Washington, Seattle. GeneReviews is a registered trademark of the University of Washington, Seattle. All rights reserved.: Seattle (WA)

Puccio H, Simon D, Cossee M, Criqui-Filipe P, Tiziano F, Melki J, Hindelang C, Matyas R, Rustin P, Koenig M (2001) Mouse models for Friedreich ataxia exhibit cardiomyopathy, sensory nerve defect and Fe-S enzyme deficiency followed by intramitochondrial iron deposits. *Nat Genet* 27: 181-186

Ritterhoff J, Tian R (2017) Metabolism in cardiomyopathy: every substrate matters. *Cardiovasc Res* 113: 411-421

Rotig A, de Lonlay P, Chretien D, Foury F, Koenig M, Sidi D, Munnich A, Rustin P (1997) Aconitase and mitochondrial iron-sulphur protein deficiency in Friedreich ataxia. *Nat Genet* 17: 215-217

Satomi Y, Hirayama M, Kobayashi H (2017) One-step lipid extraction for plasma lipidomics analysis by liquid chromatography mass spectrometry. *J Chromatogr B Analyt Technol Biomed Life Sci* 1063: 93-100

Sayles NM, Southwell N, McAvoy K, Kim K, Pesini A, Anderson CJ, Quinzii C, Cloonan S, Kawamata H, Manfredi G (2022) Mutant CHCHD10 causes an extensive metabolic rewiring that precedes OXPHOS dysfunction in a murine model of mitochondrial cardiomyopathy. *Cell Rep* 38: 110475

Shammas MK, Huang X, Wu BP, Fessler E, Song IY, Randolph NP, Li Y, Bleck CK, Springer DA, Fratter C *et al* (2022) OMA1 mediates local and global stress responses against protein misfolding in CHCHD10 mitochondrial myopathy. *J Clin Invest* 132

Tong M, Saito T, Zhai P, Oka SI, Mizushima W, Nakamura M, Ikeda S, Shirakabe A, Sadoshima J (2019) Mitophagy Is Essential for Maintaining Cardiac Function During High Fat Diet-Induced Diabetic Cardiomyopathy. *Circ Res* 124: 1360-1371

Vangaveti V, Baune BT, Kennedy RL (2010) Hydroxyoctadecadienoic acids: novel regulators of macrophage differentiation and atherogenesis. *Ther Adv Endocrinol Metab* 1: 51-60

Wai T, Garcia-Prieto J, Baker MJ, Merkwirth C, Benit P, Rustin P, Ruperez FJ, Barbas C, Ibanez B, Langer T (2015) Imbalanced OPA1 processing and mitochondrial fragmentation cause heart failure in mice. *Science* 350: aad0116

Wu T, Hu E, Xu S, Chen M, Guo P, Dai Z, Feng T, Zhou L, Tang W, Zhan L *et al* (2021) clusterProfiler 4.0: A universal enrichment tool for interpreting omics data. *Innovation (Camb)* 2: 100141

Xia W, Qiu J, Peng Y, Snyder MM, Gu L, Huang K, Luo N, Yue F, Kuang S (2022) Chchd10 is dispensable for myogenesis but critical for adipose browning. *Cell Regen* 11: 14

Zhou ZD, Saw WT, Tan EK (2017) Erratum to: Mitochondrial CHCHD-Containing Proteins: Physiologic Functions and Link with Neurodegenerative Diseases. *Mol Neurobiol* 54: 5547-5549

Figure 1.

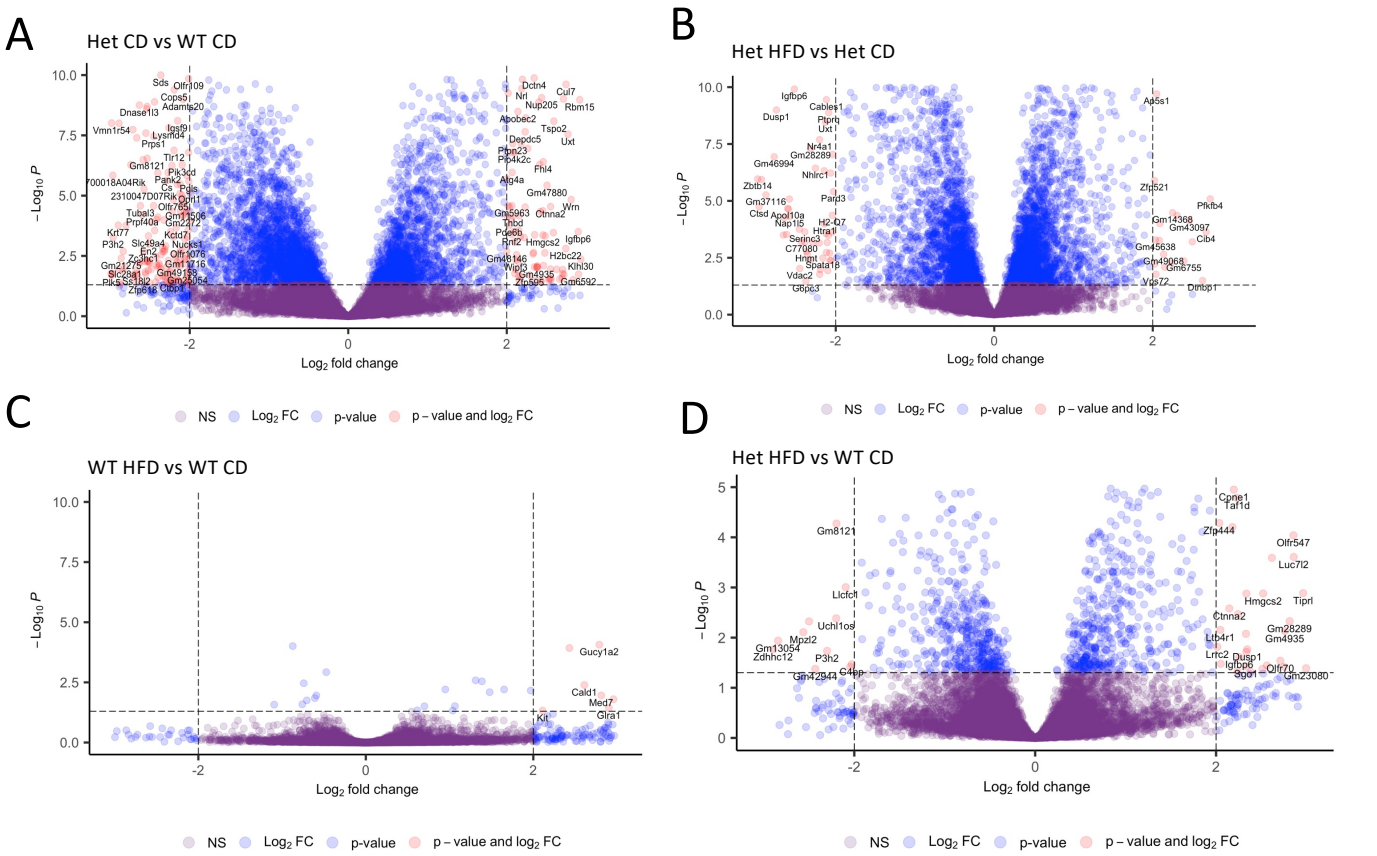
A
Het CD vs WT CD
B
Het HFD vs Het CD
C
WT HFD vs WT CD
D
Het HFD vs WT CD
$-Log_{10}$ P
Log_2 fold change
NS
Log_2 FC
p-value
p – value and log_2 FC

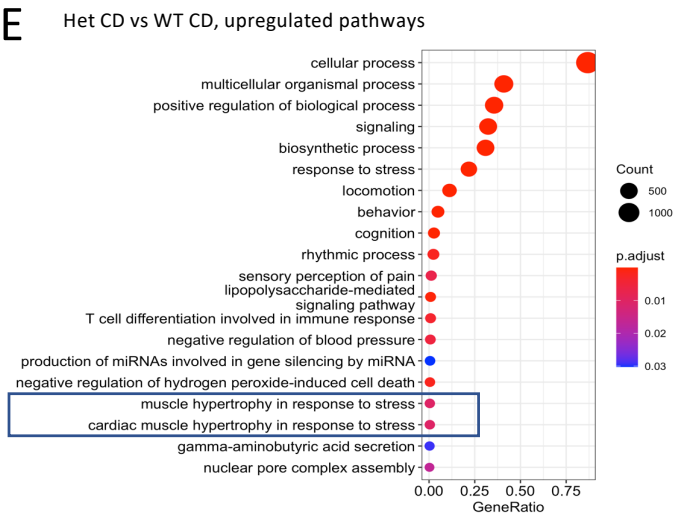
E
Het CD vs WT CD, upregulated pathways
cellular process
multicellular organismal process
positive regulation of biological process
signaling
biosynthetic process
response to stress
locomotion
behavior
cognition
rhythmic process
sensory perception of pain
lipopolysaccharide-mediated signaling pathway
T cell differentiation involved in immune response
negative regulation of blood pressure
production of miRNAs involved in gene silencing by miRNA
negative regulation of hydrogen peroxide-induced cell death
muscle hypertrophy in response to stress
cardiac muscle hypertrophy in response to stress
gamma-aminobutyric acid secretion
nuclear pore complex assembly
GeneRatio
Count
p.adjust

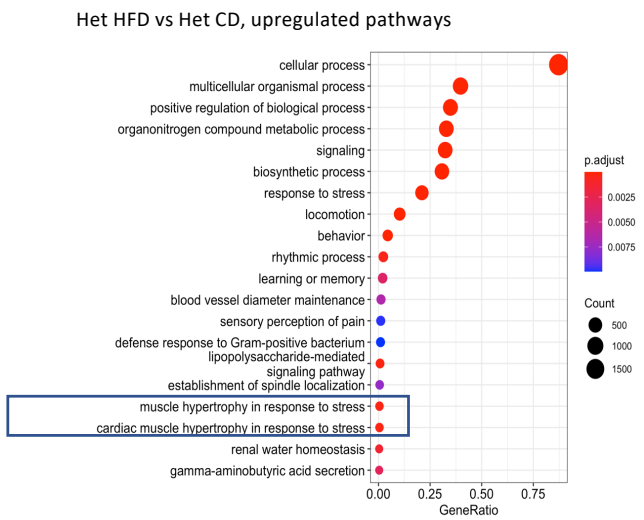
F
Het HFD vs Het CD, upregulated pathways
cellular process
multicellular organismal process
positive regulation of biological process
organonitrogen compound metabolic process
signaling
biosynthetic process
response to stress
locomotion
behavior
rhythmic process
learning or memory
blood vessel diameter maintenance
sensory perception of pain
defense response to Gram-positive bacterium
lipopolysaccharide-mediated signaling pathway
establishment of spindle localization
muscle hypertrophy in response to stress
cardiac muscle hypertrophy in response to stress
renal water homeostasis
gamma-aminobutyric acid secretion
GeneRatio
p.adjust
Count

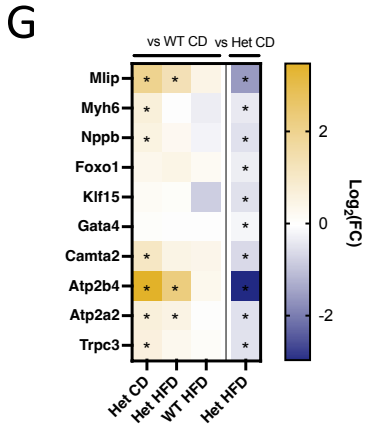
G
vs WT CD
vs Het CD
Mlip
Myh6
Nppb
Foxo1
Klf15
Gata4
Camta2
Atp2b4
Atp2a2
Trpc3
Het CD
Het HFD
WT HFD
Het HFD
$Log_2(FC)$

Figure 2.

A

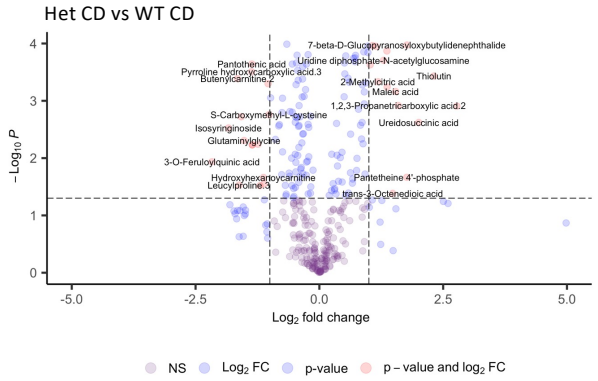

B

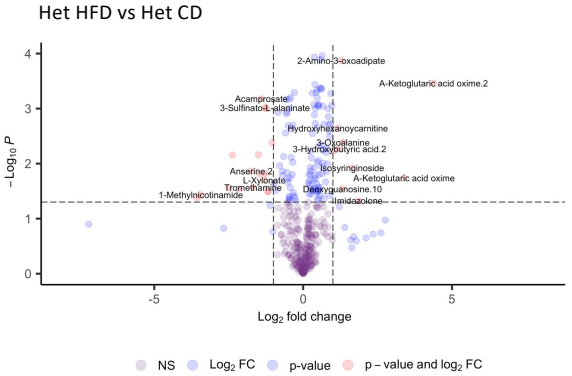

C

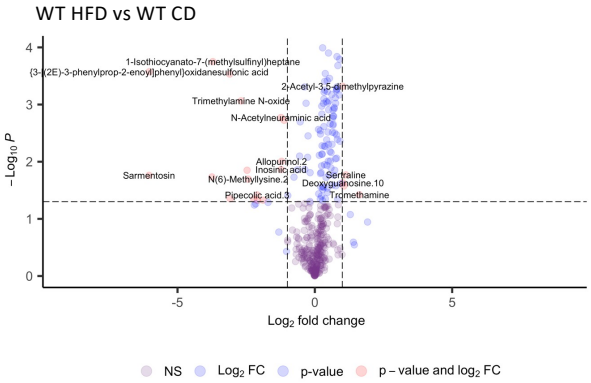

D

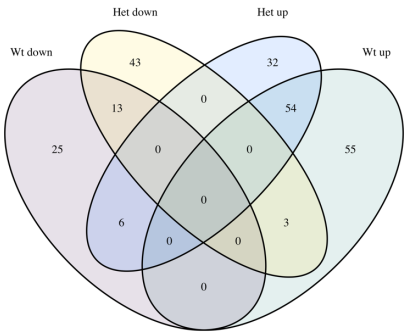

E

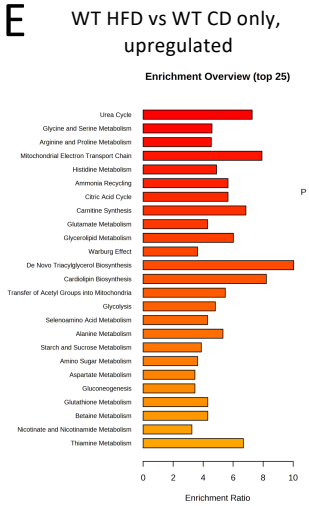

F

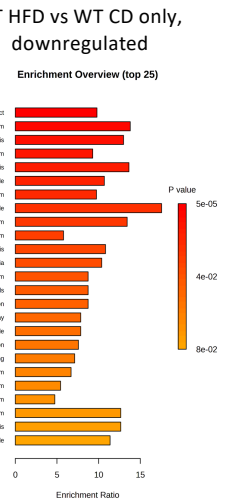

G

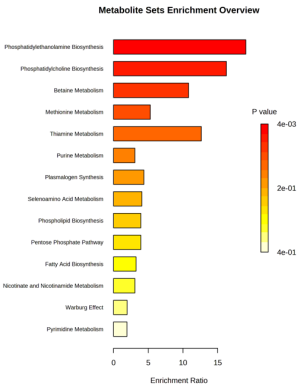

H

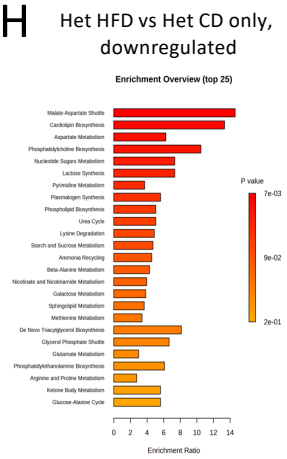

I

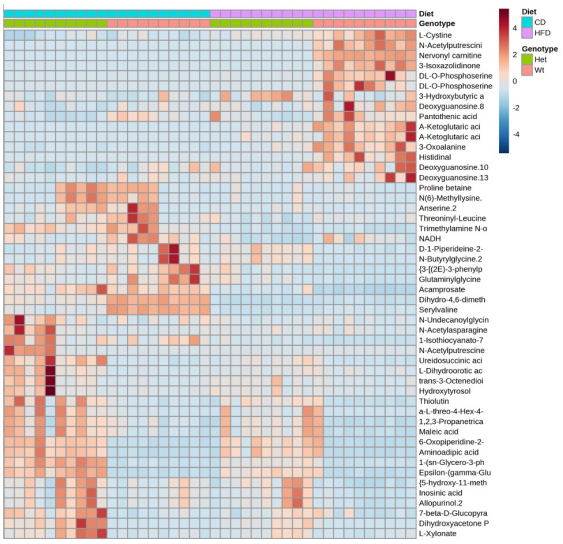

Figure 3.

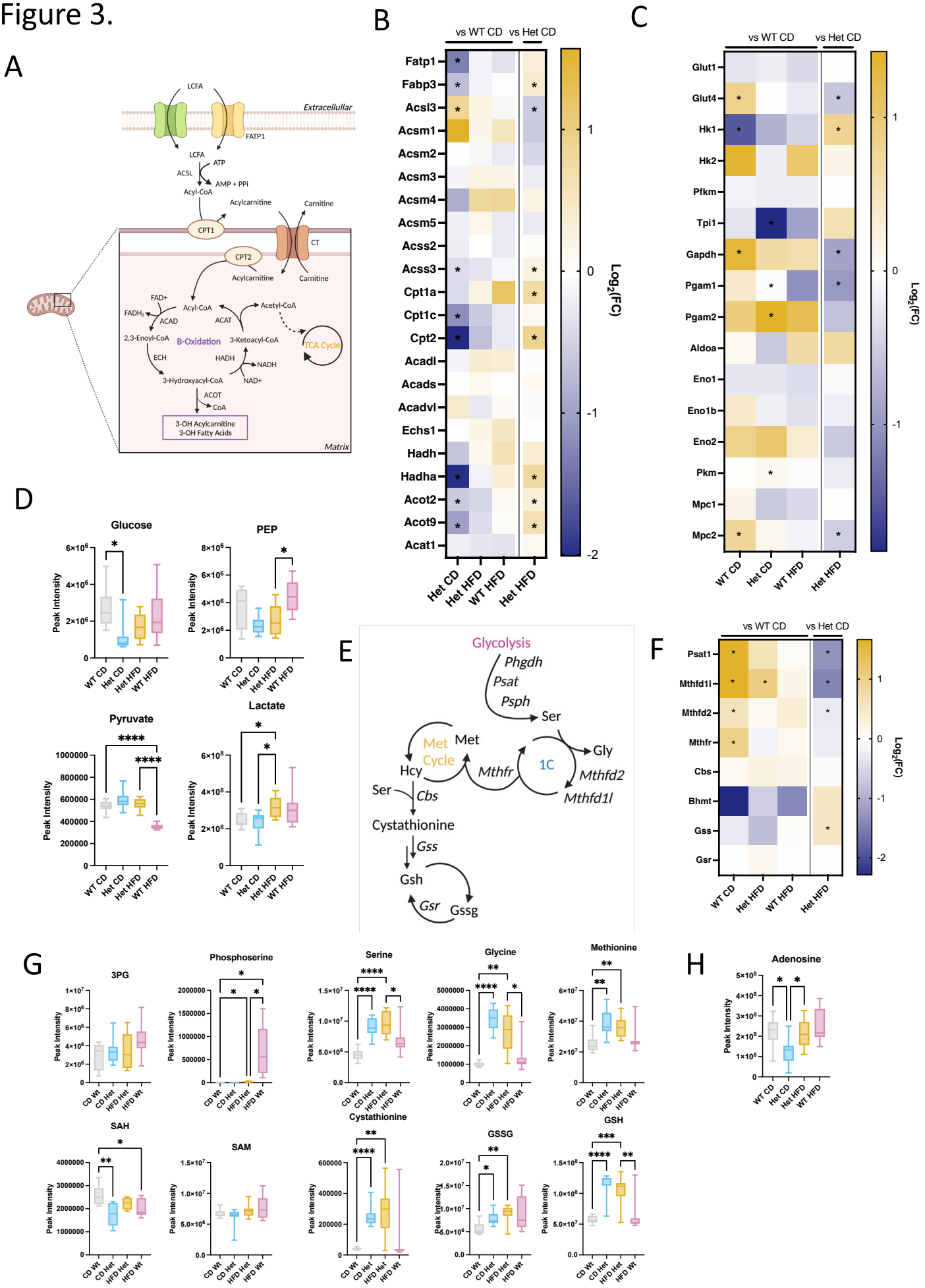
A
LCFA
Extracellular
FATP1
LCFA
ATP
ACSL
AMP + PPi
Acyl-CoA
Acylcarnitine
Carnitine
CPT1
CT
CPT2
Acylcarnitine
Carnitine
FAD+
FADH2
ACAD
Acyl-CoA
ACAT
Acetyl-CoA
2,3-Enoyl-CoA
B-Oxidation
3-Ketoacyl-CoA
TCA Cycle
ECH
HADH
NADH
3-Hydroxyacyl-CoA
NAD+
ACOT
CoA
3-OH Acylcarnitine
3-OH Fatty Acids
Matrix
B
vs WT CD
vs Het CD
Fatp1
Fabp3
Acsl3
Acsm1
Acsm2
Acsm3
Acsm4
Acsm5
Acss2
Acss3
Cpt1a
Cpt1c
Cpt2
Acadl
Acads
Acadvl
Echs1
Hadh
Hadha
Acot2
Acot9
Acat1
Log2(FC)
Het CD
Het HFD
WT HFD
Het HFD
C
vs WT CD
vs Het CD
Glut1
Glut4
Hk1
Hk2
Pfkm
Tpi1
Gapdh
Pgam1
Pgam2
Aldoa
Eno1
Eno1b
Eno2
Pkm
Mpc1
Mpc2
Log2(FC)
WT CD
Het CD
WT HFD
Het HFD
D
Glucose
PEP
Pyruvate
Lactate
Peak Intensity
WT CD
Het CD
Het HFD
WT HFD
E
Glycolysis
Phgdh
Psat
Psph
Ser
Met
Met Cycle
Hcy
Mthfr
1C
Gly
Mthfd2
Mthfd1l
Ser
Cbs
Cystathionine
Gss
Gsh
Gsr
Gssg
F
vs WT CD
vs Het CD
Psat1
Mthfd1l
Mthfd2
Mthfr
Cbs
Bhmt
Gss
Gsr
Log2(FC)
WT CD
Het HFD
WT HFD
Het HFD
G
3PG
Phosphoserine
Serine
Glycine
Methionine
SAH
SAM
Cystathionine
GSSG
GSH
Peak Intensity
CD Wt
CD Het
HFD Het
HFD Wt
H
Adenosine
Peak Intensity
WT CD
Het CD
Het HFD
WT HFD

Figure 4.

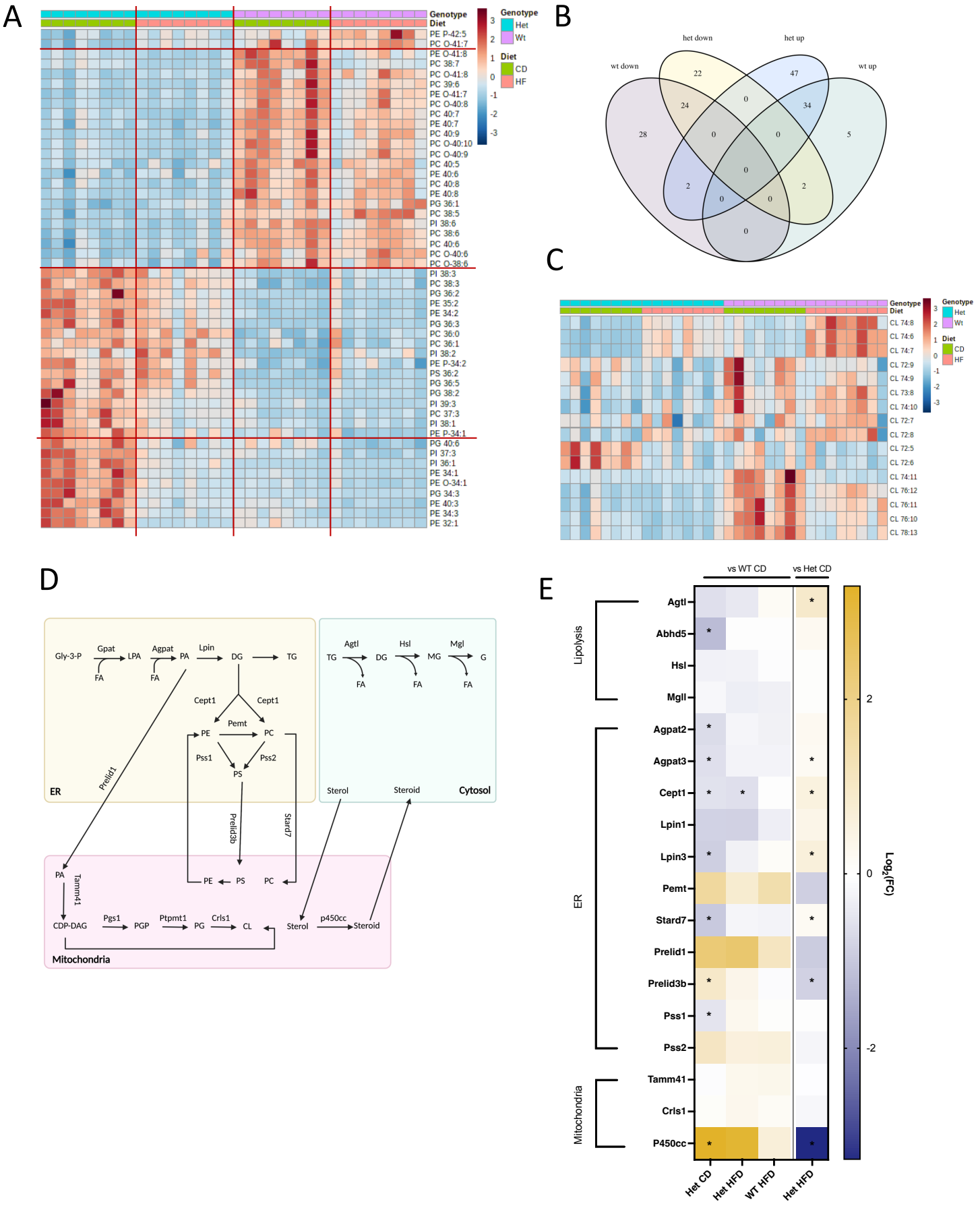
A
Genotype
Diet
Het
Wt
CD
HF
PE P-42:5
PC O-41:7
PE O-41:8
PC 38:7
PC O-41:8
PC 39:6
PE O-41:7
PC O-40:8
PC 40:7
PE 40:7
PC 40:9
PC O-40:10
PC O-40:9
PC 40:5
PE 40:6
PC 40:8
PE 40:8
PG 36:1
PC 38:5
PI 38:6
PC 38:6
PC 40:6
PC O-40:6
PC O-38:6
PI 38:3
PC 38:3
PG 36:2
PE 35:2
PE 34:2
PG 36:3
PC 36:0
PC 36:1
PI 38:2
PE P-34:2
PS 36:2
PG 36:5
PG 38:2
PI 39:3
PC 37:3
PI 38:1
PE P-34:1
PG 40:6
PI 37:3
PI 36:1
PE 34:1
PE O-34:1
PG 34:3
PE 40:3
PE 34:3
PE 32:1
B
wt down
het down
het up
wt up
22
47
24
34
28
5
2
2
0
C
CL 74:8
CL 74:6
CL 74:7
CL 72:9
CL 74:9
CL 73:8
CL 74:10
CL 72:7
CL 72:8
CL 72:5
CL 72:6
CL 74:11
CL 76:12
CL 76:11
CL 76:10
CL 78:13
D
Gly-3-P
Gpat
LPA
Agpat
PA
Lpin
DG
TG
FA
Cept1
Pemt
PE
PC
Pss1
Pss2
PS
Prelid1
ER
Agtl
Hsl
Mgl
MG
G
Sterol
Steroid
Cytosol
Prelid3b
Stard7
Tamm41
CDP-DAG
Pgs1
PGP
Ptpmt1
Crls1
CL
p450cc
Mitochondria
E
vs WT CD
vs Het CD
Lipolysis
ER
Mitochondria
Agtl
Abhd5
Hsl
Mgll
Agpat2
Agpat3
Cept1
Lpin1
Lpin3
Pemt
Stard7
Prelid1
Prelid3b
Pss1
Pss2
Tamm41
Crls1
P450cc
Het CD
Het HFD
WT HFD
Het HFD
Log2(FC)
2
0
-2

Figure 5.

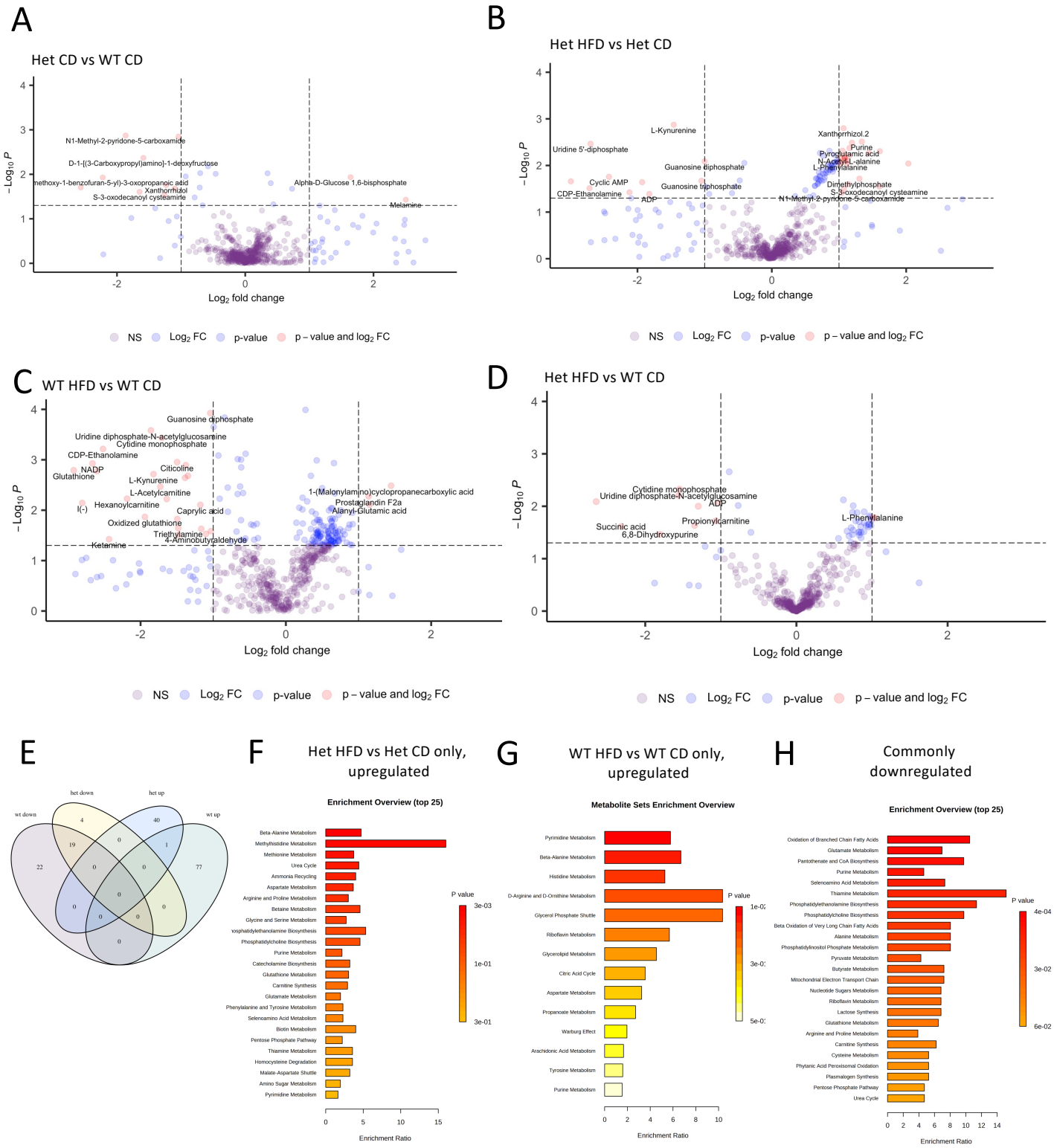
A
Het CD vs WT CD
N1-Methyl-2-pyridone-5-carboxamide
D-1-[(3-Carboxypropyl)amino]-1-deoxyfructose
methoxy-1-benzofuran-5-yl)-3-oxopropanoic acid
Xanthorrhizol
S-3-oxodecanoyl cysteamine
Alpha-D-Glucose 1,6-bisphosphate
Melamine
B
Het HFD vs Het CD
L-Kynurenine
Uridine 5'-diphosphate
Guanosine diphosphate
Cyclic AMP
Guanosine triphosphate
CDP-Ethanolamine
ADP
Xanthorrhizol.2
Purine
Pyroglutamic acid
N-Acetyl-L-alanine
L-Phenylalanine
Dimethylphosphate
S-3-oxodecanoyl cysteamine
N1-Methyl-2-pyridone-5-carboxamide
C
WT HFD vs WT CD
Guanosine diphosphate
Uridine diphosphate-N-acetylglucosamine
Cytidine monophosphate
CDP-Ethanolamine
NADP
Glutathione
Citicoline
L-Kynurenine
L-Acetylcarnitine
Hexanoylcarnitine
l(-)
Caprylic acid
Oxidized glutathione
Triethylamine
4-Aminobutyraldehyde
Ketamine
1-(Malonylamino)cyclopropanecarboxylic acid
Prostaglandin F2a
Alanyl-Glutamic acid
D
Het HFD vs WT CD
Cytidine monophosphate
Uridine diphosphate-N-acetylglucosamine
ADP
Propionylcarnitine
Succinic acid
6,8-Dihydroxypurine
L-Phenylalanine
Log10 P
Log2 fold change
NS
Log2 FC
p-value
p – value and log2 FC
E
wt down
het down
het up
wt up
F
Het HFD vs Het CD only, upregulated
Enrichment Overview (top 25)
Beta-Alanine Metabolism
Methylhistidine Metabolism
Methionine Metabolism
Urea Cycle
Ammonia Recycling
Aspartate Metabolism
Arginine and Proline Metabolism
Betaine Metabolism
Glycine and Serine Metabolism
Phosphatidylcholine Biosynthesis
Purine Metabolism
Catecholamine Biosynthesis
Glutathione Metabolism
Carnitine Synthesis
Glutamate Metabolism
Phenylalanine and Tyrosine Metabolism
Selenoamino Acid Metabolism
Biotin Metabolism
Pentose Phosphate Pathway
Thiamine Metabolism
Homocysteine Degradation
Malate-Aspartate Shuttle
Amino Sugar Metabolism
Pyrimidine Metabolism
P value
Enrichment Ratio
G
WT HFD vs WT CD only, upregulated
Metabolite Sets Enrichment Overview
Pyrimidine Metabolism
Beta-Alanine Metabolism
Histidine Metabolism
D-Arginine and D-Ornithine Metabolism
Glycerol Phosphate Shuttle
Riboflavin Metabolism
Glycerolipid Metabolism
Citric Acid Cycle
Aspartate Metabolism
Propanoate Metabolism
Warburg Effect
Arachidonic Acid Metabolism
Tyrosine Metabolism
Purine Metabolism
P value
Enrichment Ratio
H
Commonly downregulated
Enrichment Overview (top 25)
Oxidation of Branched Chain Fatty Acids
Glutamate Metabolism
Pantothenate and CoA Biosynthesis
Purine Metabolism
Selenoamino Acid Metabolism
Thiamine Metabolism
Phosphatidylethanolamine Biosynthesis
Phosphatidylcholine Biosynthesis
Beta Oxidation of Very Long Chain Fatty Acids
Alanine Metabolism
Phosphatidylinositol Phosphate Metabolism
Pyruvate Metabolism
Butyrate Metabolism
Mitochondrial Electron Transport Chain
Nucleotide Sugars Metabolism
Riboflavin Metabolism
Lactose Synthesis
Glutathione Metabolism
Arginine and Proline Metabolism
Carnitine Synthesis
Cysteine Metabolism
Phytanic Acid Peroxisomal Oxidation
Plasmalogen Synthesis
Pentose Phosphate Pathway
Urea Cycle
P value
Enrichment Ratio

Figure 6.

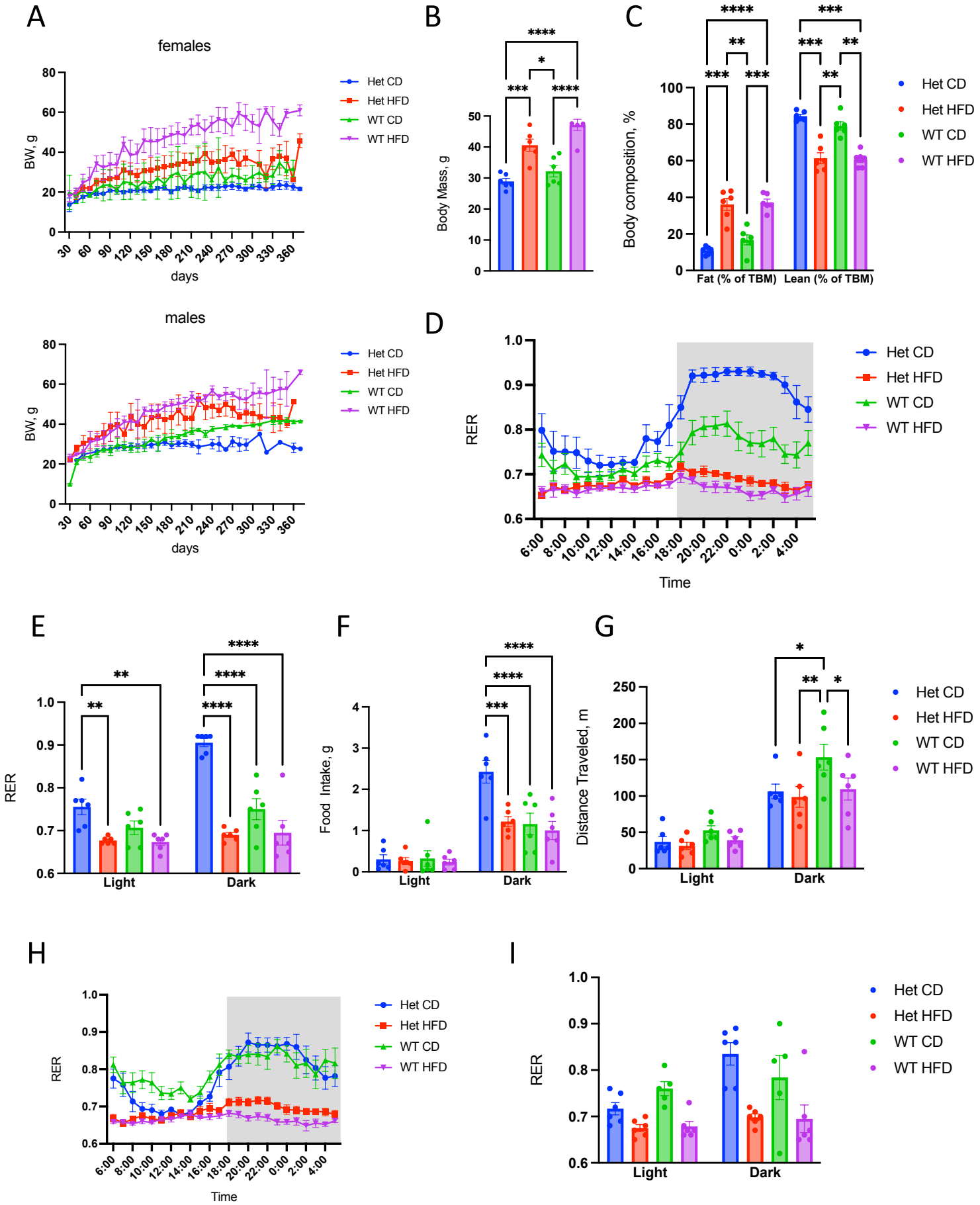
A
females
BW, g
days
Het CD
Het HFD
WT CD
WT HFD
B
Body Mass, g
C
Body composition, %
Fat (% of TBM)
Lean (% of TBM)
males
D
RER
Time
E
Light
Dark
F
Food Intake, g
G
Distance Traveled, m
H
I

Figure 7.

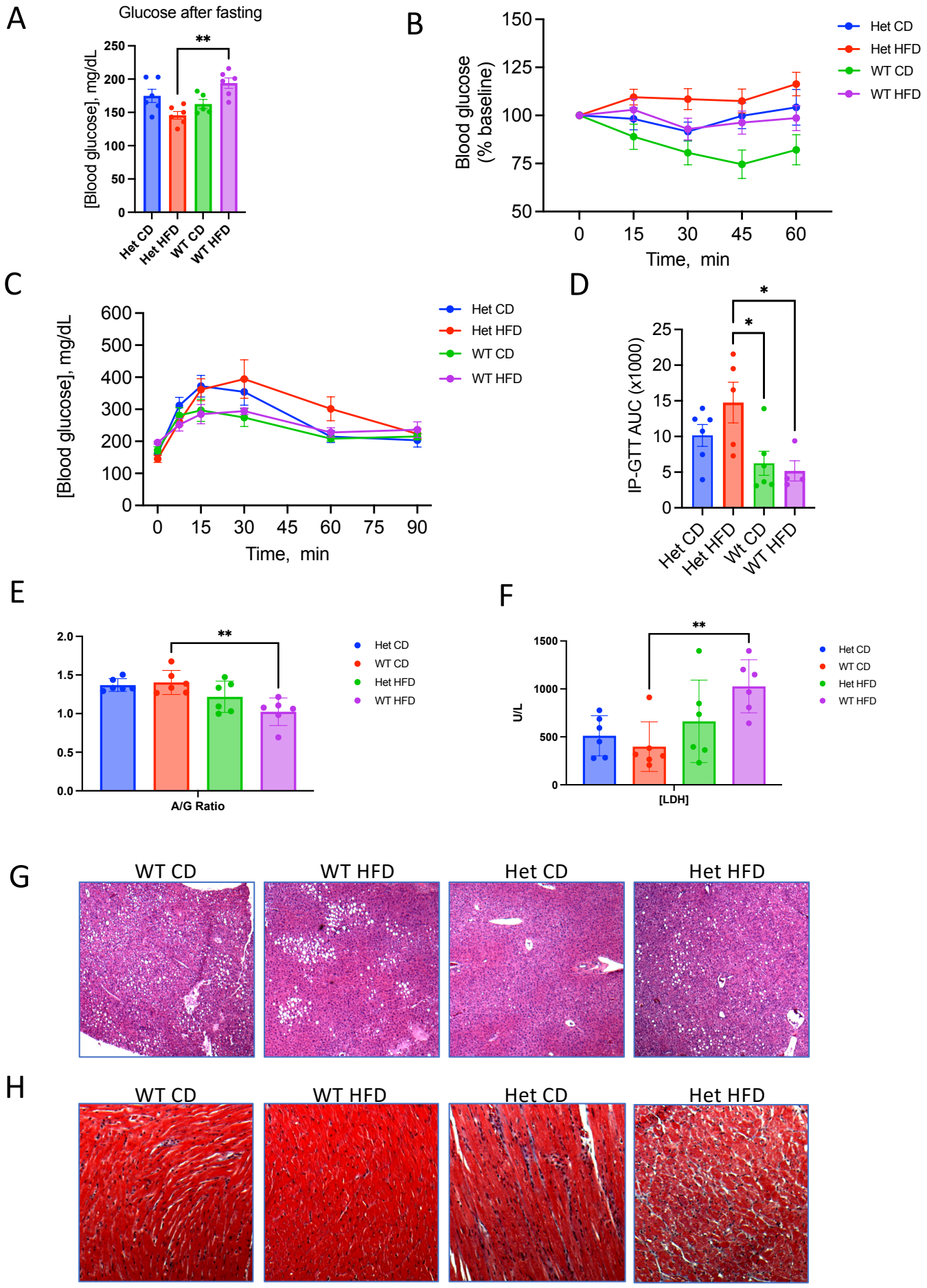
A
Glucose after fasting
[Blood glucose], mg/dL
250
200
150
100
50
0
**
Het CD
Het HFD
WT CD
WT HFD
B
Blood glucose
(% baseline)
150
125
100
75
50
0
15
30
45
60
Time, min
Het CD
Het HFD
WT CD
WT HFD
C
[Blood glucose], mg/dL
600
500
400
300
200
100
0
0
15
30
45
60
75
90
Time, min
Het CD
Het HFD
WT CD
WT HFD
D
IP-GTT AUC (x1000)
25
20
15
10
5
0
*
*
Het CD
Het HFD
Wt CD
WT HFD
E
2.0
1.5
1.0
0.5
0.0
**
A/G Ratio
Het CD
WT CD
Het HFD
WT HFD
F
U/L
1500
1000
500
0
**
[LDH]
Het CD
WT CD
Het HFD
WT HFD
G
WT CD
WT HFD
Het CD
Het HFD
H
WT CD
WT HFD
Het CD
Het HFD

Figure 8.

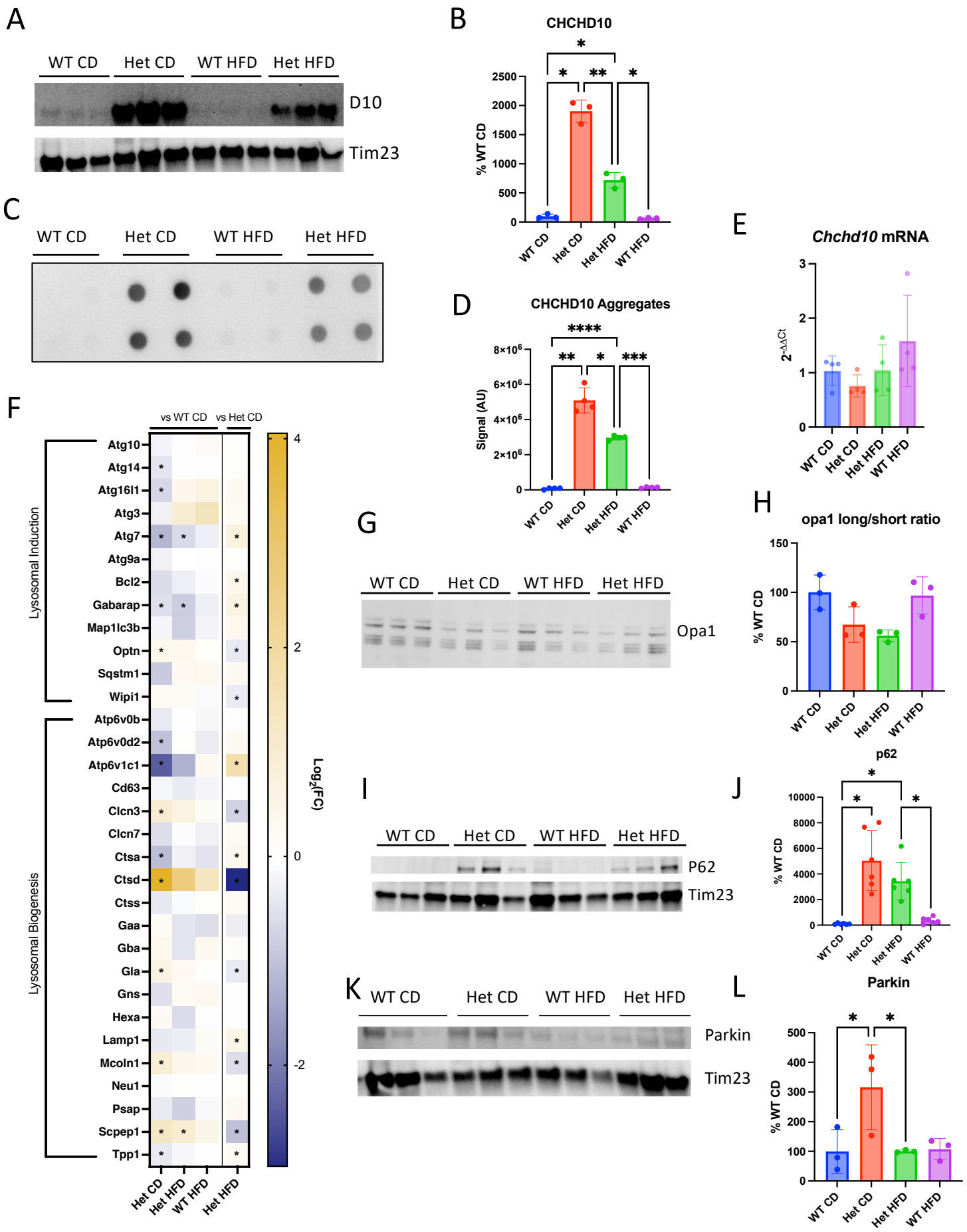
A
WT CD
Het CD
WT HFD
Het HFD
D10
Tim23
B
CHCHD10
% WT CD
C
D
CHCHD10 Aggregates
Signal (AU)
E
Chchd10 mRNA
F
vs WT CD
vs Het CD
Lysosomal Induction
Lysosomal Biogenesis
Atg10
Atg14
Atg16l1
Atg3
Atg7
Atg9a
Bcl2
Gabarap
Map1lc3b
Optn
Sqstm1
Wipi1
Atp6v0b
Atp6v0d2
Atp6v1c1
Cd63
Clcn3
Clcn7
Ctsa
Ctsd
Ctss
Gaa
Gba
Gla
Gns
Hexa
Lamp1
Mcoln1
Neu1
Psap
Scpep1
Tpp1
Log2(FC)
G
Opa1
H
opa1 long/short ratio
I
P62
J
p62
K
Parkin
L
Parkin

Figure 9.

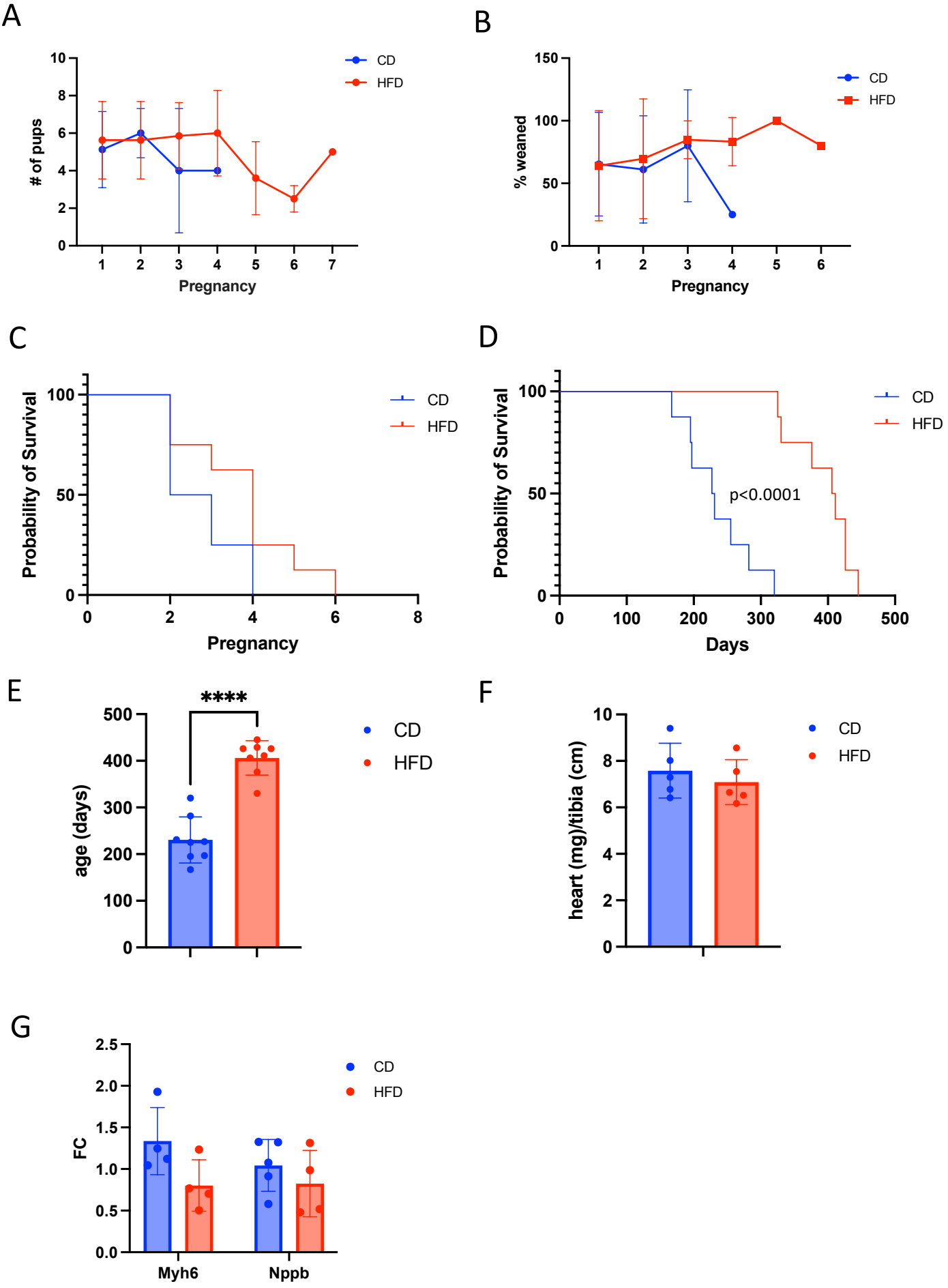
A
# of pups
Pregnancy
CD
HFD
B
% weaned
Pregnancy
CD
HFD
C
Probability of Survival
Pregnancy
CD
HFD
D
Probability of Survival
Days
p<0.0001
CD
HFD
E
****
age (days)
CD
HFD
F
heart (mg)/tibia (cm)
CD
HFD
G
FC
Myh6
Nppb
CD
HFD